Ejecta Stratigraphy Modeling of the NASA/VIPER Exploration Zone at Mons Mouton Near the Lunar South Pole

by

Hephzibah Christopher

A thesis submitted to the Graduate Faculty of
Auburn University
in partial fulfillment of the
requirements for the Degree of
Master of Science in Geology

Auburn, Alabama
May 6, 2023

Keywords: Moon, Volatiles, Ejecta, NASA VIPER

Approved by

Masatoshi Hirabayashi, Chair, Assistant Professor, Department of Aerospace Engineering,
Department of Geosciences
David King Jr., Professor, Department of Geosciences
Laura Bilenker, Assistant Professor, Department of Geosciences

Abstract

Permanently shadowed regions (PSRs) within some lunar polar craters host water ice and other volatiles delivered by sources such as asteroids, comets, interior degassing, and solar wind sputtering because of their frigid temperatures. However, over geological timescales, the abundance and spatial distribution of these ice deposits are disrupted by surface processes such as impact excavations, ejecta blanketing, and mass wasting, which cause them to be diluted and mixed with lunar regolith. To inspect their resource potential and to decode their origin and physical characteristics, NASA has planned the Volatiles Investigating Polar Exploration Rover (VIPER) to Mons Mouton near the Moon's south pole in 2024. The rover will seek ice by exploring with a 1 m drilling instrument and an array of spectrometers. In this thesis, I characterize the ejecta stratigraphy produced by small, local impact craters around the VIPER exploration site to constrain the distribution of ice and regolith within the shallow subsurface. I constructed a Monte Carlo-based ejecta deposition model that simulated the layering of ejecta produced by craters bigger than 20 m in diameter and predicted that nearly 0.9 to 59 m thick ejecta covers VIPER's primary mission area. I also determined the extent of PSRs that could host surface ice at the VIPER site by modeling long-term shadows using high-resolution topographic data. By analyzing the evolution of ejecta thickness as a function of surface age, I find that the upper 1 m of the crust, which is VIPER's drilling depth, is covered by ejecta emplaced in the last $\sim$1 billion years. Freshly supplied volatiles will likely be present in the VIPER 1 m drill cores if they have endured the effect of impact mixing and space weathering processes since deposition.

Acknowledgments

I would like to express my heartfelt gratitude to my advisor Dr. Hirabayashi, for his consistent support, mentorship and constructive criticism throughout the course of my master's program. I am thankful for believing me and for giving me the opportunity to be a part of the VIPER mission team. I extend my deep appreciation to my committee members, Dr. King and Dr. Bilenker, whose guidance and motivation throughout my research journey have been invaluable. I would like to acknowledge the members of the VIPER science team, for their insightful feedback that greatly helped shape my research. I would like to specifically thank the Department of Geosciences, for always being kind and supportive. My special gratitude goes out to my lab mates, Yaeji, Pedro, Joe and Lauren, for their friendship, encouragement, and helpful discussions that have enhanced my research experience. Many thanks to my friends who are far and near, especially to Akhila, for being a steadfast source of encouragement. Finally, I thank Amma and Annie for their unwavering support, love, and prayers. I am deeply grateful to Athai and Mama, without their endless care and understanding, this achievement would not have been possible.

Table of Contents

List of Figures

List of Tables

Chapter 1

Introduction

The presence of volatiles trapped in the permanently shaded craters of the Moon's polar regions has been a subject of great scientific interest ever since Watson et al. (1961) hypothesized their existence. Due to the heavily cratered landscape of the Moon and its slight axial tilt ($1.54°$) with respect to the ecliptic, certain polar craters are shielded from direct solar illumination and form permanently shadowed regions (PSRs), which are some of the coldest locations in the solar system (reaching temperatures as low as 40 K). As a result, these PSRs act as cold traps that preserve water ice, and other volatile species in the otherwise arid and airless lunar environment (Watson et al., 1961; Paige et al., 2010). Since the deposition of the volatiles to the polar PSRs till the present, they are destroyed, buried, and pulverized by impact cratering events, exposure to cosmic radiation, solar wind, and micrometeorites, and they become mixed with the lunar regolith (Hurley et al., 2012; Farrell et al., 2019; Costello et al., 2020). Despite the knowledge of the existence of water ice on the Moon and the prospect of harvesting it for rocket propellant production and other commercial uses (Kornuta et al., 2019; Sowers and Dreyer, 2019; Cannon and Britt, 2020; Dreyer, 2021), we still do not know its exact abundance and distribution, especially in the subsurface. NASA has planned the Volatiles Investigating Polar Exploration Rover (VIPER) robotic mission to the Mons Mouton region near the Moon's south pole in 2024 for investigating the origin, chemistry, and resource potential of lunar polar volatiles by drilling up to 1 m and testing collected samples for ice using spectrometers. In this thesis, I characterize the distribution of lunar regolith and ice in the shallow subsurface of the VIPER investigation site by modeling the material transport caused by local impact craters. There are several unexplored questions regarding the material distribution at the rover's exploration zone that will have implications for the mission's sampling experiments. How much regolith (ejecta-derived) is present across the VIPER investigation area located at Mons Mouton? What is the spatial distribution of its thickness? Where should the rover drill to successfully sample ice? What are the characteristics of regolith present in the upper 1 meter of the VIPER subsurface? Does the top 1 m of regolith contain ice?

I aim to answer the above questions by using the following methods:

1. Quantitatively predicting the ejecta thickness expected at the VIPER mission area by developing a Monte-Carlo based ejecta deposition model that simulates the stratigraphy of ejecta blankets produced by local impact craters.
2. Analyzing the evolution of ejecta thickness as a function of surface age to get insights into the possible local volatile deposition and ejecta emplacement history.
3. Delineating PSRs at the mission site by conducting long-term solar flux simulations and assessing the characteristics of ejecta inside them.

1.1 Current Understanding of Lunar Polar Volatiles

This section aims to provide a brief summary of the existing research on the deposition and evolution of water ice and other volatiles in polar cold traps and to emphasize the significance of this research work. We currently understand that lunar volatiles likely originated from three sources: impacts, volcanic degassing, and solar wind implantation. Impacting asteroids, particularly of carbonaceous type, and comets are considered to be the largest source, estimated to have supplied at least 2.7×10^{10} and 1.3×10^{8} to 4.3×10^{9} metric tons of water ice, respectively (Ong et al., 2010; Stewart et al., 2011; Prem et al., 2015). Hydrocode modeling by Ong et al. (2010) revealed that the fraction of the impactor's water mass retained by the Moon after the impact event varies with its velocity. Slow impacts tend to impart more water. When a water-bearing impactor strikes the lunar surface, the released vapor plume forms a thin, transient atmosphere that facilitates the migration of water molecules toward the polar cold traps and their subsequent condensation (Prem et al., 2015). Most of the water molecules and other volatiles delivered by impactors at any location on the Moon might be permanently lost due to impact-generated heat, while the surviving portion ballistically hops in all directions under the influence of lunar gravity until they are cold trapped (Watson et al., 1961; Butler, 1997). Transport of the surviving water molecules toward polar cold traps happens effectively on the nightside of the Moon where the surface temperature is sufficiently low to increase the residence times of the migrating molecules by inhibiting Jean's escape and photodissociation losses (Watson et al., 1961; Stewart et al., 2011; Prem et al., 2015). Micrometeoroids, which are impactors smaller than 1 cm, steadily supply water to the Moon but at quantities much lower than their larger counterparts (Grün et al., 2011; Lucey et al., 2022).

Volatiles emitted during basaltic eruption could have also considerably been trapped as polar ice. Needham and Kring (2017) proposed that the peak of lunar volcanism at 3.5 Ga could have created a transient atmosphere of 1 kPa pressure which would have lasted for at least 70 Ma. However, Head et al. (2020) argued that such a persistent atmosphere is unlikely based on the modeled shorter eruption episodes and longer intervals between eruptions, and hence, impact delivery is the major source of lunar volatiles. Nevertheless, volcanic degassing involves lower temperatures compared to impacts, thereby increasing the survival rates of the released volatiles (Kring et al., 2021). The Schrodinger cone, a prominent pyroclastic vent located near the lunar south pole, was active until 3.7 Ga and it could have substantially supplied volcanic volatiles to the south polar PSRs (Kring et al., 2021). A minor amount of water is generated when solar wind implants hydrogen onto the lunar regolith, triggering physical and chemical sputtering processes (Crider and Vondrak, 2002). The majority of volatile supply to the poles should have occurred prior to 3 Ga while impact flux rates were higher than the present and lunar volcanism was at its peak (Cannon and Britt, 2020; Lucey et al., 2022). Ice deposition modeling by (Cannon et al., 2020) predicted that the peak of ice supply to the Moon of impact origin occurred around 4 Ga, which could have produced hundreds of meters thick ice deposits in ancient polar craters. However, studies that distinguish the sources of the observed polar volatiles are lacking because of both insufficient data on their chemistry and the possibility that more than one source could have been active simultaneously. The spectrometers on board VIPER are meant to resolve this issue specifically.

After deposition, the survival of these ice masses and their spatial distribution are largely controlled by local impact cratering and space erosion processes. Aside from the slow sublimation loss of volatiles occurring inside cold traps at a rate of 1 mm/Ga (Paige et al., 2010), the ice accumulations exposed on the surface gradually erode away under the action of continuous solar particles flux and micrometeorite bombardment (Crider and Vondrak, 2002; Hurley et al., 2012; Farrell et al., 2019). Impact-induced material transport, which is responsible for the generation and mixing of regolith, is ubiquitous across the Moon (Shoemaker, 1966; Oberbeck and Quaide, 1968). At the poles, impact mixing tends to dilute and disperse the ice deposits to variable depths over geological timescales, inhibiting the existence of massive reservoirs of uncontaminated ice in the lunar PSRs. Remote mapping of the polar surfaces confirms the mixed nature of lunar ice by detecting only sparse quantities of ice homogenously mixed with regolith at variable concentrations. Li et al. (2018) detected 30 wt% ice on the surface of PSR-hosting craters by analyzing their Near Infrared (NIR) spectral signatures. Hydrogen mapping inferred from the subdued epithermal neutron flux measured by Lunar Prospector Neutron Spectrometer (LPNS) and Lunar Reconnaissance Orbiter (LRO) Lunar Exploration Neutron Detector (LEND) instruments suggests ice proportions in the range of 1.5 - 40 wt% in the upper decimeters of the surface. In the Lunar CRater Observing and Sensing Satellite (LCROSS) impact experiment which excavated materials from $\sim$5 m depth (Schultz et al., 2010) on the floor of the permanently shadowed crater Cabeus, only 5 wt% ice was detected in the ejecta plume (Colaprete et al., 2010). Radar backscatter signals which evidently pointed out the presence of pure ice at the Mercurian poles, failed to do so at the lunar poles, asserting the mixed nature of lunar ice (Neish et al., 2011; Thomson et al., 2012). These empirical results amplify the need to investigate the true abundance of lunar volatiles by assessing the effect of impact mixing on ice-rich surfaces. Though bulky deposits are hypothesized to be present in the subsurface of polar craters (Rubanenko et al., 2019; Cannon et al., 2020) buried under crater ejecta, we are yet to understand the variation in ice abundance with depth.

Ejecta blankets of impact craters bury surface ice and preserve them from erosion while impact excavations bring the buried deposits to the surface, causing exposure to the hostile lunar environment, thereby significantly depleting them. The combination of these processes is known as ‘impact gardening’ and it is predicted to have dehydrated the polar cold traps in the upper 1- 3 m (Costello et al., 2018, 2020, 2021). Additionally, gardening would have occurred concurrently with the ice supply, limiting the pristine buildup of ice in the cold traps (Costello et al., 2020). Nonetheless, buried ice could also have been excavated to the surface by recent impacts and still not completely depleted by gardening, explaining the surface ice exposures observed by Li et al. (2018). By employing impactor flux rates and crater scaling parameters, impact gardening is quantified by probabilistic models in terms of the number of times the material present at depth is excavated by impacts over a time period (Gault et al., 1974; Costello et al., 2018). While gardening models are effective in placing constraints on the extent of ice removal on a global scale, they require enhancement to describe the depth distribution characteristics of ice and regolith at a specific location which might be of interest to in-situ exploration or extraction attempts. The ejecta distribution model developed in this work uses the empirical crater population at the VIPER site, which will more accurately characterize materials present in the shallow subsurface.

1.2 VIPER Rover Exploration

While the scientific importance of lunar water ice has been highlighted ever since its discovery, its potential as a space resource has been recently contemplated through various computational and conceptual studies (Sowers and Dreyer, 2019; Cannon and Britt, 2020; Dreyer, 2021). One of the core objectives of the NASA Artemis missions is to utilize lunar volatiles through In-Situ Resource Utilization (ISRU) for sustaining long-term lunar exploration and deep space missions (NASA, 2020a). As a forerunner to Artemis, NASA has planned to deploy the VIPER rover to the south pole of the Moon in 2024 to survey water ice distribution and its physical characteristics (NASA, 2020b; Colaprete, 2022; Colaprete et al., 2023). It will be the first resource prospecting mission to be implemented outside of Earth. VIPER will utilize three ice prospecting instruments namely Mass Spectrometer Observing Lunar Operations (MSolo), Near-Infrared Volatiles Spectrometer System (NIRVSS) which are capable of sensing ice at the surface, and Neutron Spectrometer System (NSS) which can detect up to 80 cm depth (Colaprete, 2022). It will also excavate up to 1 m depth using The Regolith and Ice Drill for Exploring New Terrains (TRIDENT) and the collected samples will be probed by MSolo and NIRVSS for ice signatures. Additionally, the rover's accelerometer can conduct seismic sounding up to 5 m depth.

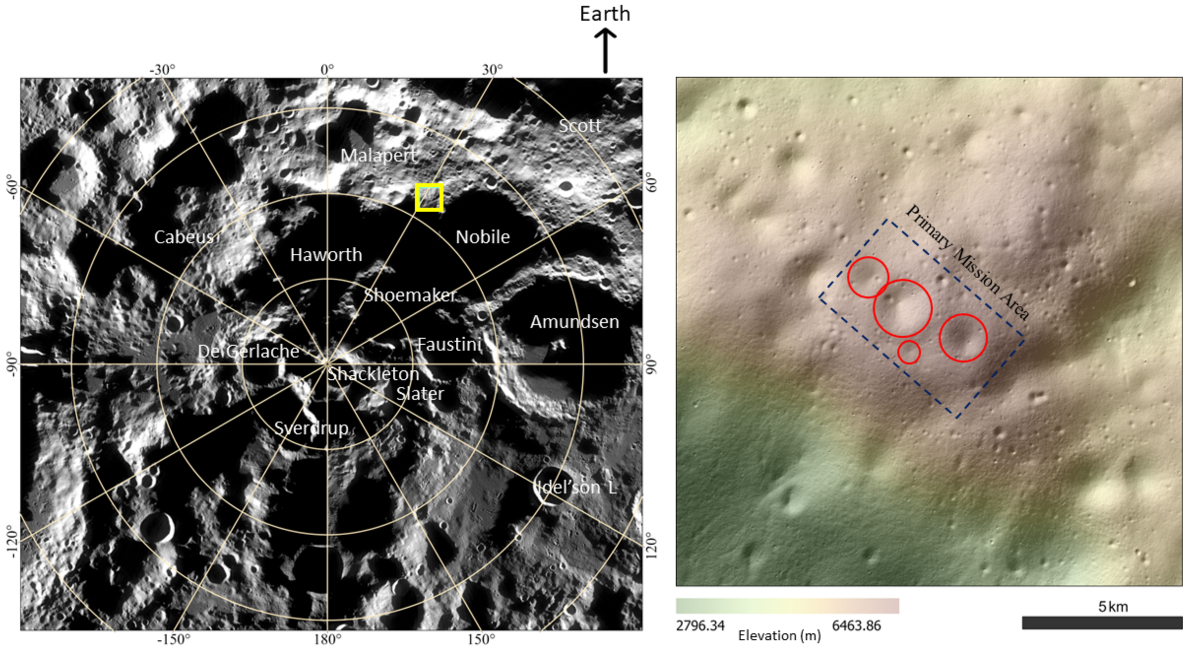

Figure 1.1: Lunar Reconnaissance Orbiter Camera (LROC) Wide Angle Camera (WAC) map of the Moon's south pole shown on the left with large craters labeled. The study area 'Mons Mouton' containing the VIPER landing site is bounded by the yellow box. The figure on the right is a 5 m per pixel resolution Digital Elevation Model (DEM) overlain on a hillshade map. VIPER's primary mission area (dashed box) is in the middle of the study site. Fassett et al. (2022) estimated the ages of craters (marked by red circles) in the primary area to be older than 3.6 Ga.

The rover will land at Mons Mouton ($-85.42°$ N, $31.62°$ E) located at the western rim of the Nobile crater (Figure 1.1), traverse the PSRs, then collect and analyze drill cores over a period of 3 lunar days (100 Earth days). The ice resource maps prepared by VIPER data will be crucial in establishing future ISRU operations and in the formulation of effective mining methods. The investigation site is favored because of its elevated topography, which offers continuous solar illumination to some locations where the rover could reside during lunar nights. The site also has steady Earth visibility needed for communication. The primary mission area has four large PSR hosting craters (shown as red circles in Figure 1.1) that formed 3.6 Ga ago and several smaller, younger (< 1 Ga) PSRs possibly containing freshly delivered ice (Fassett et al., 2022). Mapping the spatial and depth distribution of regolith and ice at the landing area is vital to assist VIPER in successfully sampling lunar water.

Chapter 2

Methodology

This chapter has two sections that elucidate the computational techniques employed to accomplish the objectives of this work. In the first section, I describe the construction of a Monte-Carlo-type model that predicts ejecta characteristics of the study area and the collection of crater data given as input to the model. The second section explains the development of an illumination model that delineates permanently shadowed regions in the study area.

2.1 Monte Carlo Modeling of Ejecta Thickness Distribution across the VIPER site

2.1.1 Mapping Impact Crater Population at the VIPER Site

The first step of modeling the ejecta thickness characteristics at the study area is to map all the impact craters located on it. Using a Lunar Orbiter Laser Altimeter (LOLA) derived DEM of the study grid having a 5 m/pixel spatial resolution (Barker et al., 2021), I created shaded relief maps at different solar incidence angles and used them along with the slope map of the region to manually map its impact crater population. The usage of shaded relief maps provides false illumination throughout the study area, including the PSRs, thus enabling us to visualize the craters located there that are otherwise not visible in optical imagery. Additionally, by adjusting the solar incidence of these maps to higher angles, the brightness contrasts between relief features can be enhanced, which makes even shallower crater rims easy to detect. Crater counting was carried out using the 2-point tool in the CraterTools toolkit in ArcMap. I did not differentiate primaries from secondaries in the counting process since both kinds of cratering produce ejecta blankets and influence the stratigraphy of the Moon's surface. 28922 craters with diameters greater than 8 m were initially counted. The Cumulative Size Frequency Distribution (CSFD) curve for the initial count shown in Figure 2.1b, flattens at diameters smaller than 20 m which indicates bias when counting smaller craters. So, I eliminated craters smaller than 20 m, and 24862 craters of diameters 20 m to 4.3 km (shown as red circles in Figure 2.1a) were considered for ejecta modeling.

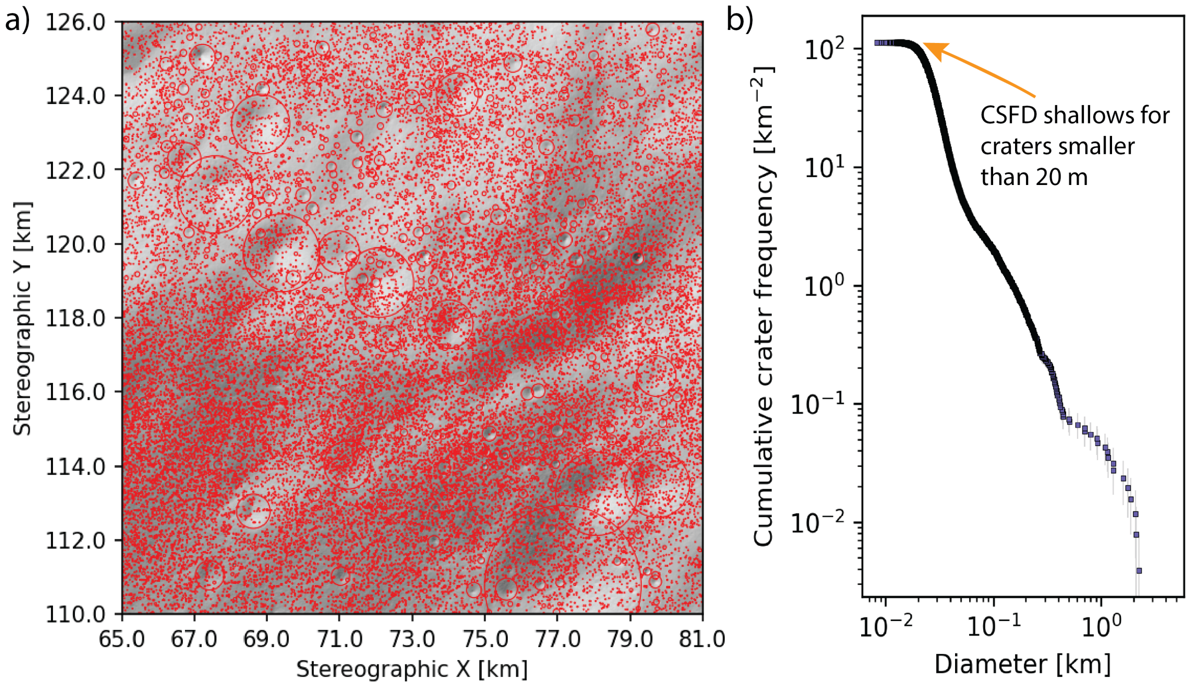

Figure 2.1: a) Impact craters larger than 20 m at the study site are shown as red circles. b) CSFD plot for the entire crater count data (28922 craters). The shallow slope portion of the curve (shown by the arrow) indicates the counting bias for craters smaller than 20 m.

2.1.2 Ejecta Blanketing Simulations

Impact bombardment on a solid surface generates shock waves that propagate hemispherically through the target surface, causing the excavation of crustal materials and their subsequent ejection in upward and outward directions at subsonic velocities (Melosh, 1989). The ejected debris ballistically deposits around the impact site in the form of an ejecta blanket whose thickness falls off exponentially away from the crater rim. McGetchin et al. (1973) expressed the thickness of the ejecta blanket t as a function of radial distance r from the crater rim as

$$t = \begin{cases} T\,(\frac{r}{R})^{\beta}, & \text{if } r \geq R \\ 0, & \text{if } r < R \end{cases} \tag{2.1}$$

Here, the exponent, $\beta = 3$ denotes the decrease in the thickness of the blanket with range and R is the crater radius. Ejecta occurring over the rim of the crater is the thickest part of the blanket and it is expressed by T in Equation 2.1. All measurements are in meter units. McGetchin et al. (1973) calculated T as $0.14\,R^{0.74}$. Pike (1974) modified the expression of T as $0.033\,R$ based on their empirical analysis of small, simple crater morphometry. Since the impact craters mapped across the study area in Section 2.1.1 are of simple crater category, I used Pike's expression to determine their ejecta blanket thicknesses in the ejecta blanketing model.

A simulation grid of 16 × 16 km area where each grid cell is of 5 × 5 m dimensions (identical to the 5 m/px DEM used for crater counting in Section 2.1.1) is considered. Though CSFD measurements reveal the age of a cratered terrain, the reconstruction of the actual impact history using CSFD is too complex. So, I opt to apply the Monte Carlo technique to model the ejecta stratigraphy of the visible craters at the study site. At the beginning of the simulation, the model grid is assigned flat topography and a zero initial ejecta thickness. At each simulation step, craters counted across the grid are emplaced in their respective locations on the grid but their sequence of emplacement is chosen randomly. After each crater emplacement, the thickness of its ejecta blanket is computed using Pike's ejecta thickness equation. Once a crater is formed on the grid, the ejecta thickness accumulated within its interior is removed before progressing to the next model step. The mean ejecta thickness of the grid is calculated by finding the total ejecta volume collected in the grid and dividing it by the grid area at each step. Likewise, the mean ejecta thickness of the primary mission area is also derived.

2.1.3 Surface Age Determination using Poisson Timing Analysis

To understand variation in ejecta thickness growth through time, I estimate the age of the study grid surface during each model step based on the density of the craters accumulated on the grid till that step. Crater densities observed across the Moon's surfaces are indicators of the duration of exposure to cosmic impacts since their formation and hence, widely employed in dating techniques together with the use of the Lunar production function and the Lunar chronology function. Radiometric ages of samples collected during the Apollo and Luna missions are correlated with their corresponding crater frequencies to formulate the lunar chronology function (Neukum, 1983) which is expressed as:

$$C(t) = b_1[e^{(b_2 t)} - 1] + b_3 t \tag{2.2}$$

Here $C(t)$ represents the number of craters larger than or equal to 1 km in diameter accumulated within a 1 km^2 area in t billion years. $b_1 = 5.44 \times 10^{-14}$, $b_2 = 6.93$ and $b_3 = 8.38 \times 10^{-4}$ are the coefficients. The lunar production function is the ideal size-frequency distribution (SFD) of craters forming at any time on the Moon's surface. Neukum (1983) describes it as an 11th-degree polynomial function (equation 2.3) that gives the cumulative number of craters $N(D)$ larger than and equal to a specified diameter D that formed in a unit area per unit time.

$$N(D) = log_{10}(N) = \sum_{j=0}^{11} a_j \times [log_{10} D)]^j \tag{2.3}$$

a_0 through a_{11} are coefficients whose values are taken from Ivanov et al. (2001). The traditional approach to age dating involves fitting the production function to the CSFD-style representation of crater density data which makes the age results dependent on the type of binning chosen, and the type of data presentation (cumulative, differential) and it also requires a minimum count. Poisson Timing Analysis described in Michael et al. (2016) relies on Poisson probability and Bayesian inference to obtain a statistically robust age estimate and I choose to apply this technique in this study. Michael et al. (2016) express the age of a surface as the probability of occurrence of the counted crater population during a time period t,

$$P(k,\lambda)=\frac{\lambda^k}{k!}e^{-\lambda} \tag{2.4}$$

In the above equation, P is the Poisson probability mass function that expresses the probability of occurrence of k number of cratering events, and λ is the known average cratering rate. λ is a function of crater diameter and can be expressed as:

$$\lambda_i = A[N(d_i^{min}) - N(d_i^{max})] \tag{2.5}$$

where N is the cumulative number of craters calculated from equation 2.3 for a set of observed craters (i) with a small diameter interval δd. d^{min} and d^{max} are the diameters at either end of the interval. Let us consider the crater population emplaced on the study grid till a model step s as $\mathbb{D}$. $\mathbb{D}$ is divided into n number of bins. The probability of occurrence of $\mathbb{D}$ is the product of the probabilities of occurrence of the individual bins.

$$pr(\mathbb{D},t)=\prod_{i=1}^{n} P(k_i,\lambda_i(t)) \tag{2.6}$$

Michael et al. (2016) applied Bayesian inference to define a function that describes the likelihood of the given crater population occurring during a specific age. Since $\mathbb{D}$ is being divided into n bins, not all of these intervals may contain craters and some might be empty, particularly if n is large. Taking this into account, the likelihood function can be written as:

$$pr(\mathbb{D},t)=\frac{\prod_{i=1}^{n} P(k=0,\lambda_i(t))}{\prod_{d_i\in\mathbb{D}} P(k=0,\lambda_i(t))}\prod_{d_i\in\mathbb{D}} P(k=1,\lambda_i(t)) \tag{2.7}$$

In the above equation, the fractional part represents empty diameter bins ($k=0$) and the second part represents diameter bins containing craters. Substituting P from equation 2.4,

$$pr(\mathbb{D},t)=\frac{\prod_{i=1}^{n} e^{-\lambda_i(t)}}{\prod_{d_i\in\mathbb{D}} e^{-\lambda_i(t))}}\prod_{d_i\in\mathbb{D}} \lambda_i(t)e^{-\lambda_i(t))} \tag{2.8}$$

$$pr(\mathbb{D},t) = \prod_{i=1}^{n} e^{-\lambda_i(t)} \prod_{d_i \in \mathbb{D}} \lambda_i(t) \tag{2.9}$$

Substituting λ_i from equation 2.5 and simplifying the above equation, we get the probability of the occurrence of the observed crater configuration in terms of their diameters and production function at a time t.

$$pr(\mathbb{D},t) \propto \exp\Big(-A[N(d,t)]_{d_{min}}^{d_{max}}\Big)[N(d=1,t)]^{n_{\mathbb{D}}} \tag{2.10}$$

where $n_{\mathbb{D}}$ is the number of craters in $\mathbb{D}$. $pr(\mathbb{D},t)$ is computed by varying t from 4.5 Ga to 0 Ga (present) in small intervals, and the value of t which yields the median of the probability density function is concluded as the age of the surface. The timescales corresponding to the 34$\%$ and 68$\%$ on either side of the median are assigned as error bars to the age estimate. In each step of the Monte Carlo model, the craters added to the grid so far are arranged in the increasing order of their diameters, and the largest 4 craters are considered as $\mathbb{D}$ and used for age estimation. Ages estimated at the end of every model step are used in determining the temporal evolution of ejecta growth.

2.2 Illumination modeling

An illumination model is constructed to measure the incident solar radiation at the VIPER site to constrain the regions that are in permanent shadow. Solar flux density reaching the surface of the Moon is given by

$$e(d) = \frac{L}{4\Pi d^2} \tag{2.11}$$

where d is the Sun - Moon distance in meters and $L = 3.8275 \times 10^{26}\, W$ is the nominal solar luminosity. The standard solar flux reaching the Earth is $1361\, W/m^2$. Owing to the Moon's 1.54° obliquity with respect to the ecliptic plane, the solar flux striking its polar regions is inclined and it can be determined as

$$e^*(d) = e(d)\, \cos\theta \tag{2.12}$$

where θ is the solar incidence angle given as the cosine of a dot product between the Sun vector $\vec{u}$ and normal to the surface $\vec{n}$. It proportionates to the fraction of solar flux reaching the surface. $\vec{u}$ is a 3-D unit vector pointing from the Sun to the Moon derived as

$$\vec{u} = \frac{\vec{X_m} - \vec{X_s}}{|\vec{X_m} - \vec{X_s}|} \tag{2.13}$$

$\vec{X_s}$ and $\vec{X_m}$ are position vectors of the Sun and the Moon respectively in the Moon Mean Earth (Moon_ME) body fixed frame as observed from the solar system barycenter. Moon_ME frame (shown in Figure 2.2a) is a planetocentric right-handed coordinate frame with its positive X axis pointing toward the center of Earth, positive Z axis along the Moon's spin axis, and the positive Y axis perpendicular to X and Z axes.

Next, for the calculation of surface normal vectors in the 16 km x 16 km VIPER site, I used a LOLA-derived high-resolution DEM of 5 m/px spatial resolution. It is referenced to the south-polar stereographic projection. ϕ and λ are latitude and longitude of each surface cell. r is elevation measured from the center of the Moon. The spatial coordinates (ξ, η, ζ) of each surface cell in the Moon_ME coordinate frame are extracted from the input DEM raster. Georeferenced rasters contain a set of 6 coefficients (listed in Table 2.1) that are obtained using the Geospatial Data Abstraction Library (GDAL) library. These coefficients are used to convert image coordinates (rows, columns) to a georeferenced coordinate system by applying the affine transformation.

Symbol	Parameter	value
$xoff$	stereographic X coordinate of the upper left corner of the upper left pixel	65000.0 [m]
a	west to east pixel resolution	5.0 [m]
b	row rotation	0.0
$yoff$	stereographic Y coordinate of the upper left corner of the upper left pixel	126000.0 [m]
d	column rotation	0.0
e	north to south pixel resolution	-5.0 [m]

Table 2.1: Geotransform coefficients of the VIPER site DEM.

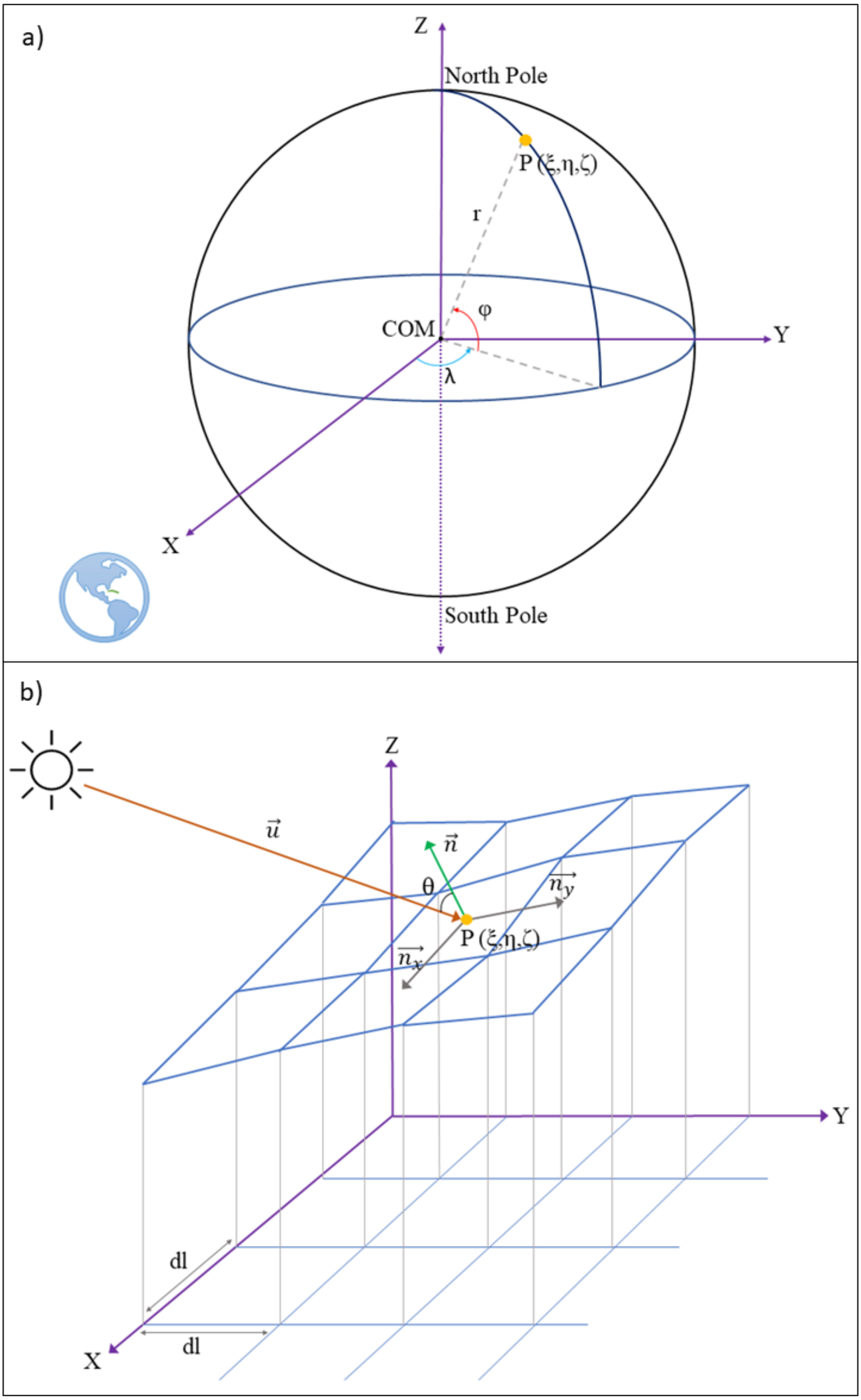

Figure 2.2: Coordinate frame and vectors used in the illumination model. Panel (a) shows the body-centered Moon_ME coordinate frame with a point P located on the surface at a distance r from the center of the Moon (COM). P has (ξ, η, ζ) coordinates along X, Y, and Z axes respectively. Panel (b) illustrates the lunar surface topography as a blue-colored mesh. The normal vector $\vec{n}$ at P is computed as the cross product of surface gradients, $\vec{n_x}$ and $\vec{n_y}$, and the Sun's direction is given by $\vec{u}$. θ is the solar incidence angle which is usually higher at the poles.

Row and column rotation coefficients are zero and north-south resolution is negative because the raster is facing North up. The affine transformation described in equations 2.14 and 2.15 is applied to compute the stereographic X and Y coordinates (X_s, Y_s) of all the surface cells.

$$X_s = a \times j + b \times i + xoff \tag{2.14}$$

$$Y_s = d \times j + e \times i + yoff \tag{2.15}$$

where i and j are the row and column indices of each pixel in the DEM raster. The next step is to convert the stereographic X and Y coordinates to the Moon_ME coordinate frame in spherical format (ϕ and λ) using the below conversions.

$$\phi = sin^{-1}(\cos c \sin \phi_1 + \frac{\sin c \cos \phi_1}{\rho}) \tag{2.16}$$

$$\lambda = \lambda_0 + tan^{-1}(\frac{X_s \sin c}{\rho \cos \phi_1 \cos c - Y_s \sin \phi_1 \sin c}) \tag{2.17}$$

where

$$\rho = \sqrt{{X_s}^2 + {Y_s}^2} \tag{2.18}$$

$$c = 2\,tan^{-1}(\frac{\rho}{2R}) \tag{2.19}$$

R is the radius of the lunar reference sphere and it is 1737.4 km. ϕ_1 and λ_0 are the latitude and longitude of the center of projection which is the South pole in this case. Therefore, $\phi_1 = \frac{-\pi}{2}$ and $\lambda_0 = 0$. The z-surface coordinate r in the Moon_ME is the distance of each surface cell from the COM and it is the sum of R and the DEM elevation of each cell. The spherical Moon_ME coordinates (ϕ, λ, r) are converted to their respective cartesian form (ξ, η, ζ). The last step is carried out because the solar vector $\vec{u}$ is also in cartesian format.

Gradients along X and Y directions are

$$\vec{n_x} = (\frac{\frac{\partial \xi}{\partial x}}{\sqrt{(\frac{\partial \xi}{\partial x})^2}}, \frac{\frac{\partial \eta}{\partial x}}{\sqrt{(\frac{\partial \eta}{\partial x})^2}}, \frac{\frac{\partial \zeta}{\partial x}}{\sqrt{(\frac{\partial \zeta}{\partial x})^2}}) \tag{2.20}$$

$$\vec{n_y} = (\frac{\frac{\partial \xi}{\partial y}}{\sqrt{(\frac{\partial \xi}{\partial y})^2}}, \frac{\frac{\partial \eta}{\partial y}}{\sqrt{(\frac{\partial \eta}{\partial y})^2}}, \frac{\frac{\partial \zeta}{\partial y}}{\sqrt{(\frac{\partial \zeta}{\partial y})^2}}) \tag{2.21}$$

The unit normal to a surface cell is

$$\vec{n} = \frac{\vec{n_x} \times \vec{n_y}}{|\vec{n_x} \times \vec{n_y}|} \tag{2.22}$$

Equation 2.23 computes the dot product between the solar vector $\vec{u}$ obtained in Equation 2.13 and the surface normal vector $\vec{n}$ computed in the above step (Equation 2.22), which gives the cosine of incidence angle at each cell that can be plotted as a hillshade map.

$$Mhill = \cos\theta = -\vec{u} \,.\, \vec{n} \tag{2.23}$$

A surface cell is shaded by itself when the Sun is below the horizon (i.e., when the solar incidence angle is greater than $\pi/2$). Therefore, cells with negative $Mhill$ values are zeroed out.

Once self-shading effects are eliminated, shadows cast by terrain relief are modeled. A shadow mapping algorithm is developed that checks if each cell (called the ‘affecting cell’) is obstructing another cell (called the ‘affected cell’) from the sun ray (Figure 2.3). This is achieved by tracing any cell of lower elevation present along the affecting cells using a tile that moves in the direction opposite to the Sun’s position. If an affected cell traced in the anti-Sun direction has a higher elevation than the affecting cell, it is sunlit. Otherwise, the affected cell is in shadow. The algorithm is implemented in two steps.

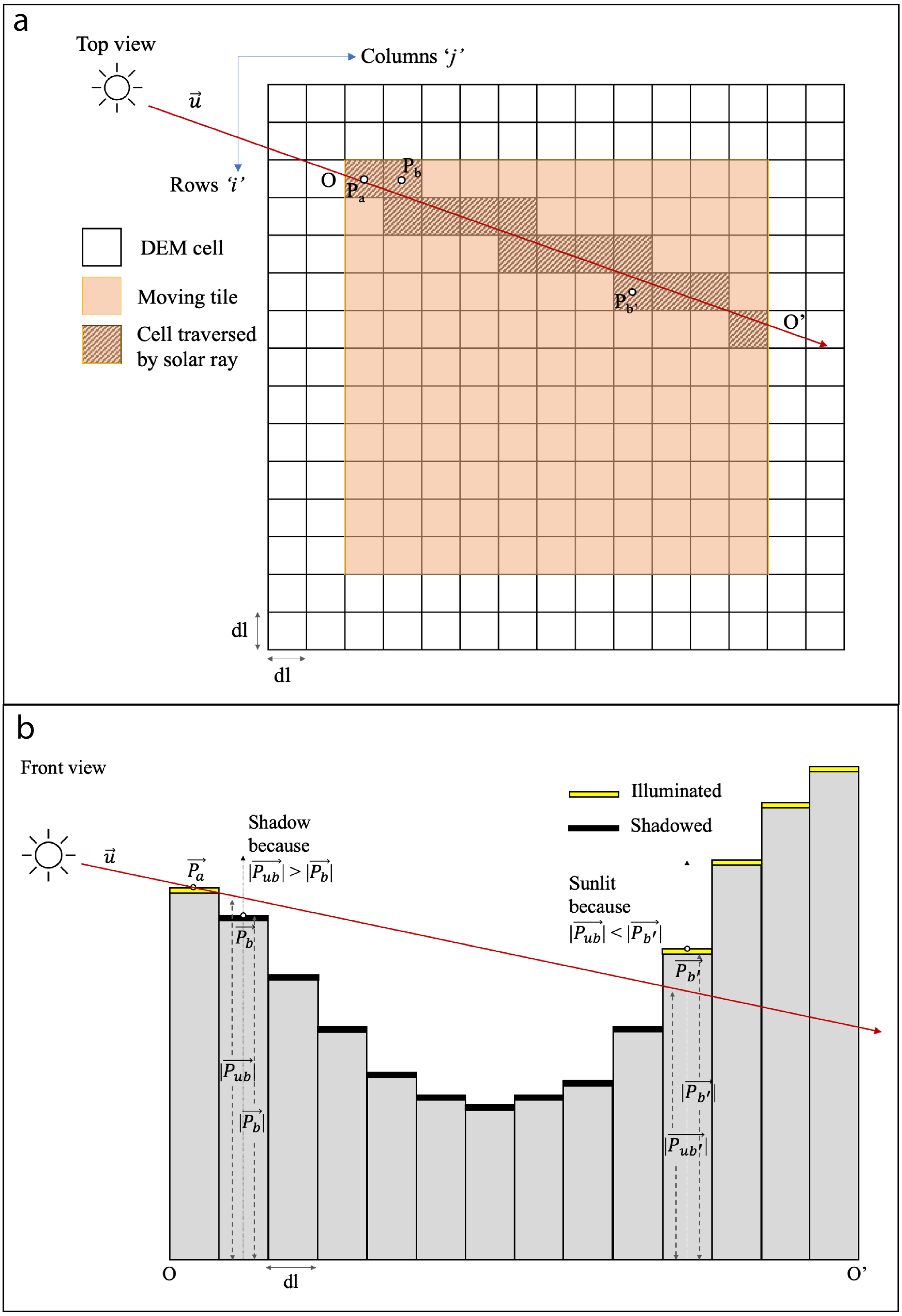

Figure 2.3: Illustrations depicting the components and working of the shadow mapping algorithm. Panel (a) depicts solar ray tracing done in Step 1. The transect O-O’ gives the DEM cells traversed by the horizontal Sun ray which are obtained using the moving tile. Panel (b) demonstrates the shading of affected cells P_b and P_b' by the affecting cell P_a in the O-O’ transect in Step 2. P_a obstructs P_b whose elevation is lower than the solar ray while P_b' being higher than the solar ray is not obstructed by P_a. Illuminated cells are indicated in yellow and the shaded cells in black.

Step 1: Solar ray tracing.

To find the traverse path of the sunray over the DEM, only the horizontal components of the Sun's position vector are considered. $\vec{us}$ is the 2D unit Sun position vector consisting only of X and Y coordinates in the lunar body fixed Moon_ME frame. $\vec{us}$ is then translated to Python array indexing, where rows correspond to the negative X axis and columns correspond to the positive Y axis. $\vec{us}_x$ and $\vec{us}_y$ are x and y components of $\vec{us}$. An affecting cell is defined as $\vec{P_a}$ whose X, Y, Z coordinates in the Moon_ME frame are given by $\xi_a(i_a, j_a)$, $\eta_a(i_a, j_a)$ and $\zeta_a(i_a, j_a)$ respectively. i_a and j_a are row and column indices respectively (Figure 2.3a).
An affected cell $\vec{P_b}$ along the moving tile is defined as $\{\xi_b(i_b, j_b), \eta_b(i_b, j_b), \zeta_b(i_b, j_b)\}$. $\vec{P_b}$ is located in anti-Sun direction to $\vec{P_a}$ at indices i_b and j_b which are derived from a shifting parameter α_b and the indices of $\vec{P_a}$ as follows:

$$i_b = i_a + \alpha_b \vec{us}_x \tag{2.24}$$

$$j_b = j_a + \alpha_b \vec{us}_y \tag{2.25}$$

The shifting parameter α_b is computed based on tile size and number of iterations.

Step 2: Comparing cell elevations.

Figure 2.3b illustrates Step 2. Let $\vec{n_b}$ be the unit vector of $\vec{P_b}$.

$$\begin{aligned}\vec{n_b} = \{&\frac{\xi_b(i_b, j_b)}{\sqrt{\xi_b(i_b, j_b)^2 + \eta_b(i_b, j_b)^2 + \zeta_b(i_b, j_b)^2}}, \frac{\eta_b(i_b, j_b)}{\sqrt{\xi_b(i_b, j_b)^2 + \eta_b(i_b, j_b)^2 + \zeta_b(i_b, j_b)^2}}, \\ &\frac{\zeta_b(i_b, j_b)}{\sqrt{\xi_b(i_b, j_b)^2 + \eta_b(i_b, j_b)^2 + \zeta_b(i_b, j_b)^2}}\}\end{aligned} \tag{2.26}$$

Height of the affected pixel $\vec{P_b}$ is calculated as $\mid \vec{P_b} \mid = \vec{n_b} \, . \, \vec{P_b}$. Let $\vec{P_{u_b}}$ be the point where the Sun ray intersects $\vec{P_b}$ along the Z direction. $\vec{P_{u_b}}$ has the same X and Y components as $\vec{P_b}$. Z component zu_b of the point $\vec{P_{u_b}}$ is given by,

$$zu_b = \zeta_a(i_a, j_a) + l_{ab} \vec{u_z} \tag{2.27}$$

where $l_{ab} = \sqrt{(\xi_a(i_a, j_a) - \xi_b(i_b, j_b))^2 + (\eta_a(i_a, j_a) - \eta_b(i_b, j_b))^2}$ is the distance between $\vec{P_a}$ and $\vec{P_b}$ and, $\vec{u_z}$ is the Z component of the 3D Sun position vector. Height of $\vec{P_{u_b}}$ is calculated as $\mid \vec{P_{u_b}} \mid = \vec{n_b} \, . \, \vec{P_{u_b}}$.

If $\mid \vec{P_{u_b}} \mid > \mid \vec{P_b} \mid$, then $\vec{P_b}$ is in shadow of $\vec{P_a}$.

$$Mhill(i_b, j_b) = \begin{cases} Mhill(i_b, j_b), & \text{if } \mid \vec{P_{u_b}} \mid \leq \mid \vec{P_b} \mid \\ 0, & \text{if } \mid \vec{P_{u_b}} \mid > \mid \vec{P_b} \mid \end{cases} \tag{2.28}$$

After estimating shadows across the site, the incident solar flux at each pixel is computed by multiplying standard solar flux with $Mhill$ (Equation 2.12).

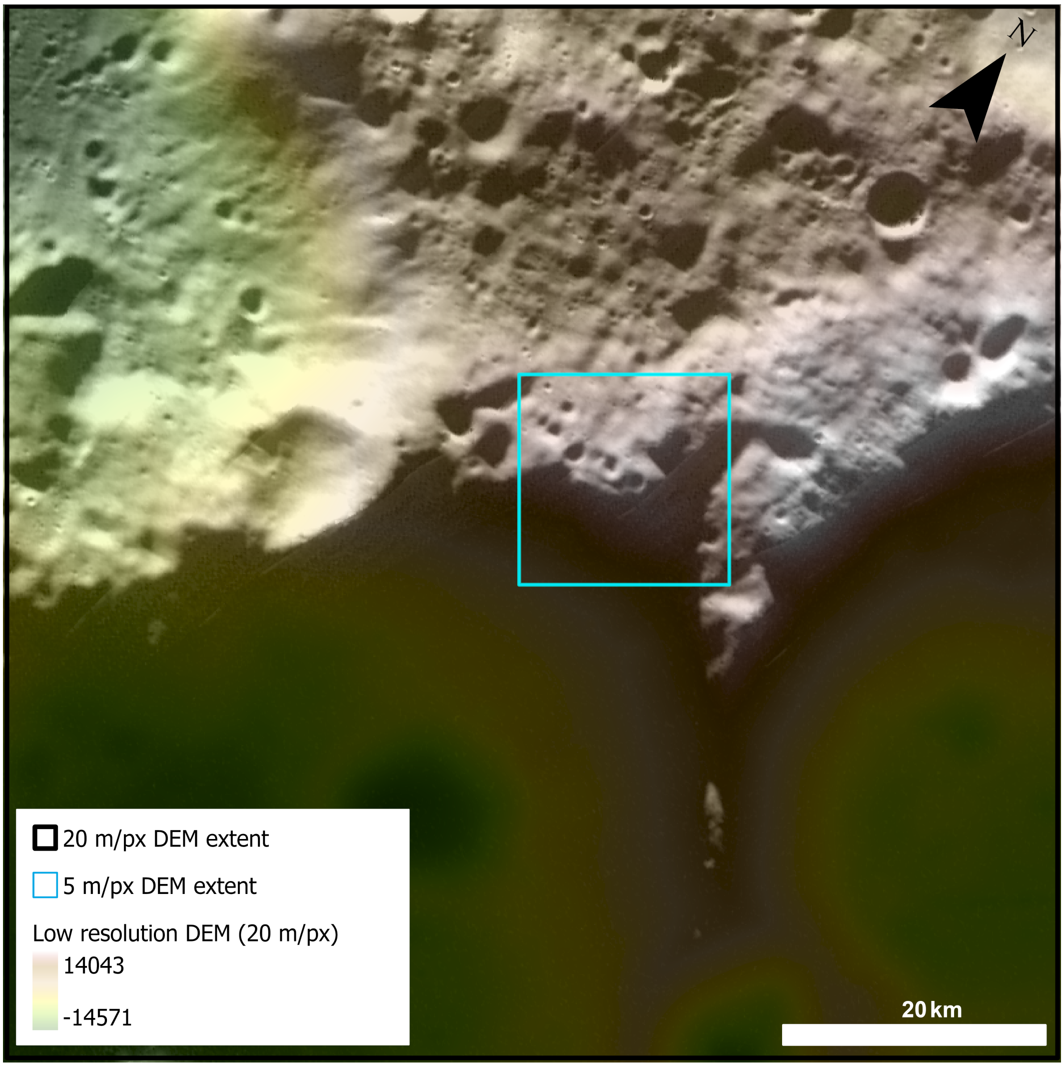

Figure 2.4: Map of the broader extent of topography surrounding the VIPER site considered in the shadow model. The cyan box placed near the middle is the location of the 16 × 16 km study site area for which the high-resolution DEM is used.

Distant topography (located outside the 16 × 16 km grid extent) also cast shadows at the study site. To integrate such distant shadows, I used a low-resolution DEM (20 m/px) resolution that covers a larger area of the Moon's south pole, centered near the extent of the VIPER site 5 m/px DEM. The spatial extents of the low (20 m/px) and high (5 m/px) resolution DEMs are shown in Figure 2.4. Shadows are computed for the low-resolution DEM using a moving tile of size 1500 × 1500 which means that the search distance for shadow-casting cells is 30 km. In the case of the high-resolution DEM, the tile size is 500 × 500 which refers to a search distance of 2.5 km. The shadows computed using the low-resolution DEM are then mapped onto the high-resolution grid. The shadow model is written in Python using NumPy, Scipy, and SpiceyPy libraries. Spiceypy, the SPICE package for Python (Annex et al., 2020) is used to compute the positions of the Sun and the Moon for any given UTC. SPICE toolkit requires NASA's NAIF (Navigation and Ancillary Information Facility) kernels, which are files containing ancillary information about planetary bodies. The kernels used in this model are listed in Table 2.2.

Kernel name	Description	File
Spacecraft and planetary ephemeris kernel	stores the positions and velocities of planets and satellites in binary format	*de421.bsp*
Planetary constants kernel	contains physical constants required to define the lunar body frame	*moon_pa_de421_1900-2050.bpc*
Frame kernel	defines lunar reference frames in ASCII format	*moon_080317.tf*
Leapsecond kernel	provides information about the leap seconds introduced to UTC and enables accurate time computation	*naif0009.tls*

Table 2.2: NAIF kernels used in shadow computation.

Chapter 3

Results

This chapter details the results produced by the models described in the previous chapter. The map of the permanently shadowed regions of the study grid derived from the illumination model is explained in Section 3.1. The outcomes of the ejecta blanketing model are presented in Section 3.2. In Section 3.3, the ejecta growth rate obtained from the ejecta model is compared with its analytical derivation using Hirabayashi et al. (2018).

3.1 PSRs at the VIPER Exploration Region

The illumination model is validated by running simulations for UTCs at which LRO Narrow Angle Camera (NAC) images of the study area were captured and comparing the simulation results with the orbital images. NAC images from 8 different dates between 2009 and 2015 were used for validation. A strong agreement between past lunar shadows and the simulated shadows is observed for all the UTCs chosen for the validation process and a few of them are displayed in Figure 3.1. The illumination model is run over a period of one lunar precessional cycle ($\sim$18.6 years) and the average solar flux reaching the VIPER site is computed (shown in Figure 3.2). Cells with zero average solar flux are marked to be in permanent shadow. Figure 3.3 shows the PSR map of the VIPER site. About 3.5% (9 km^2) of the study grid and 2.3% ($\sim$0.5 km^2) of the primary mission area are permanently shadowed. Stable ice can exist on the surface of these regions and if present, it will be detected by the prospecting instruments onboard the VIPER rover.

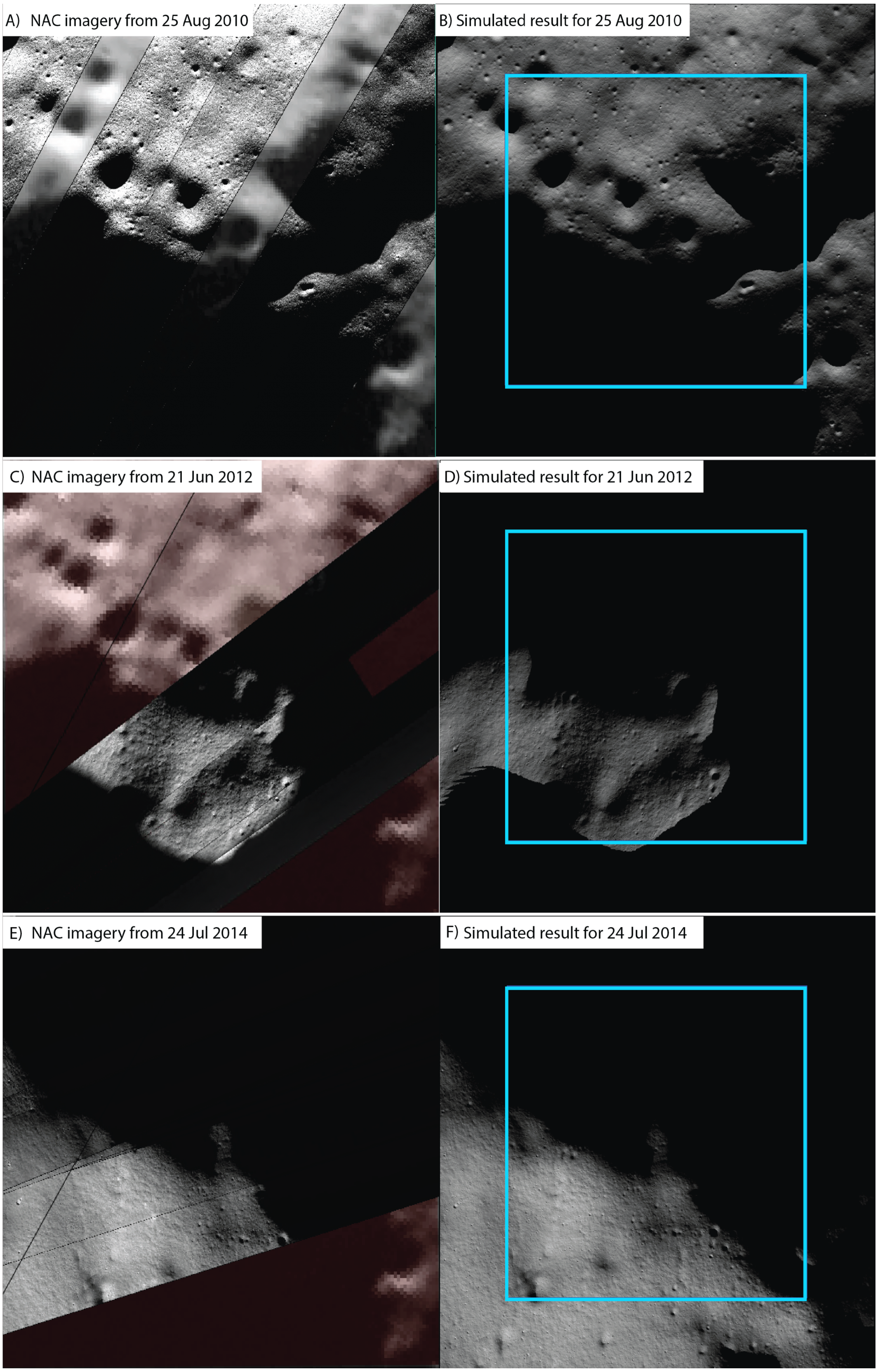

Figure 3.1: The left column (A, C, E) shows spacecraft imagery of the VIPER site captured by the LRO NAC optical camera on different dates and their corresponding simulated outputs are on the right (B, D, F). The high-resolution (50 cm/px) NAC strips overlay a coarser base map on the left images. The blue box placed on the simulated images shows the extent of the model output which is free from the moving tile's buffer effect. The cells lying outside the blue box did not have enough cells within the moving tile in all directions which could have led to less reliable shadow tracing.

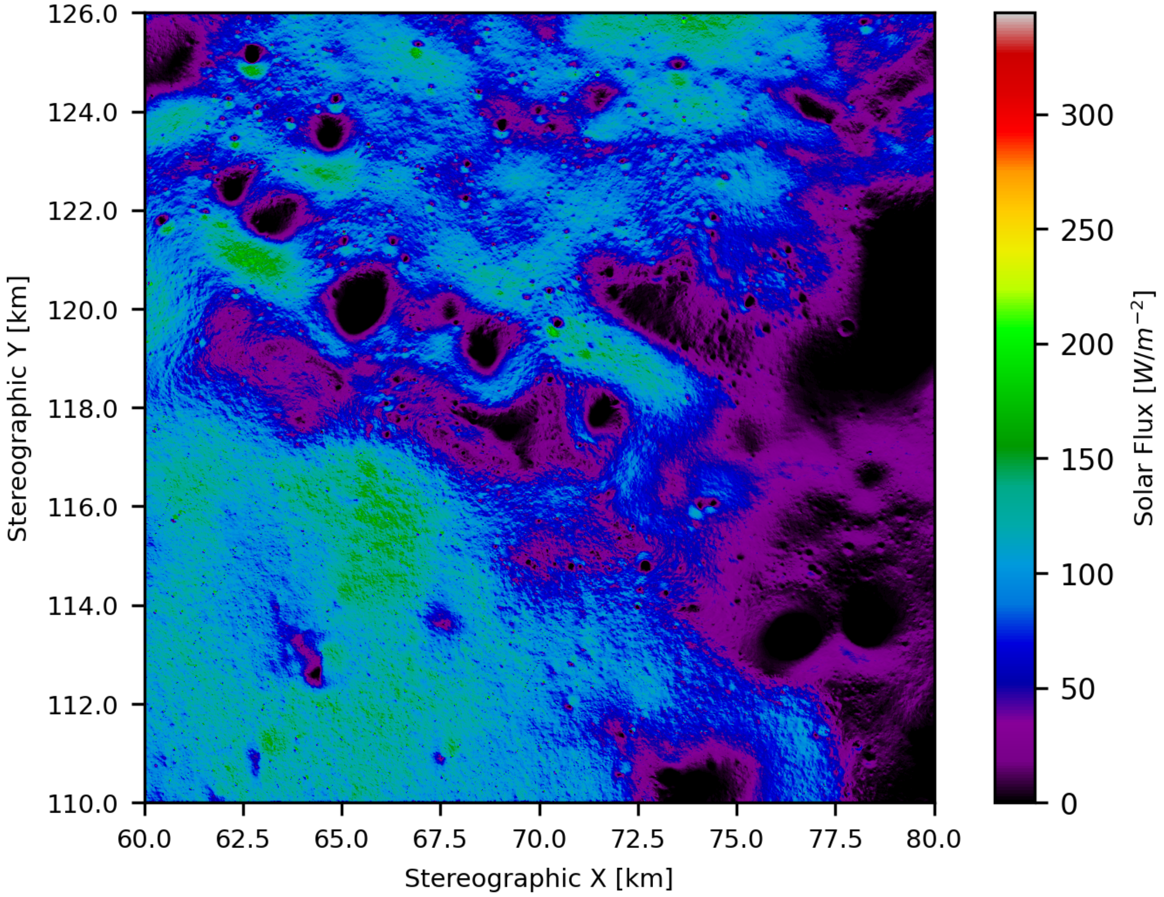

Figure 3.2: Map showing the distribution of incident solar flux at the study site averaged over 18.6 years. The X and Y spatial coordinates are in south-polar stereographic projection.

Most of the PSRs are observed on crater floors rather than the inter-crater plains. The sizes of the PSRs depend on the sizes and slope characteristics of the crater floors. Like the slope dichotomy, the southern slopes of the study grid do not have larger PSRs. The primary mission area has two PSRs larger than 0.1 km^2 and several small-scale ones. It should be noted that the PSR boundaries derived from the illumination model are slightly larger than their actual extents because the model does not incorporate scattered flux exuded by illuminated slopes. Such scattered light causes the edges of the PSRs to be brightened to some extent.

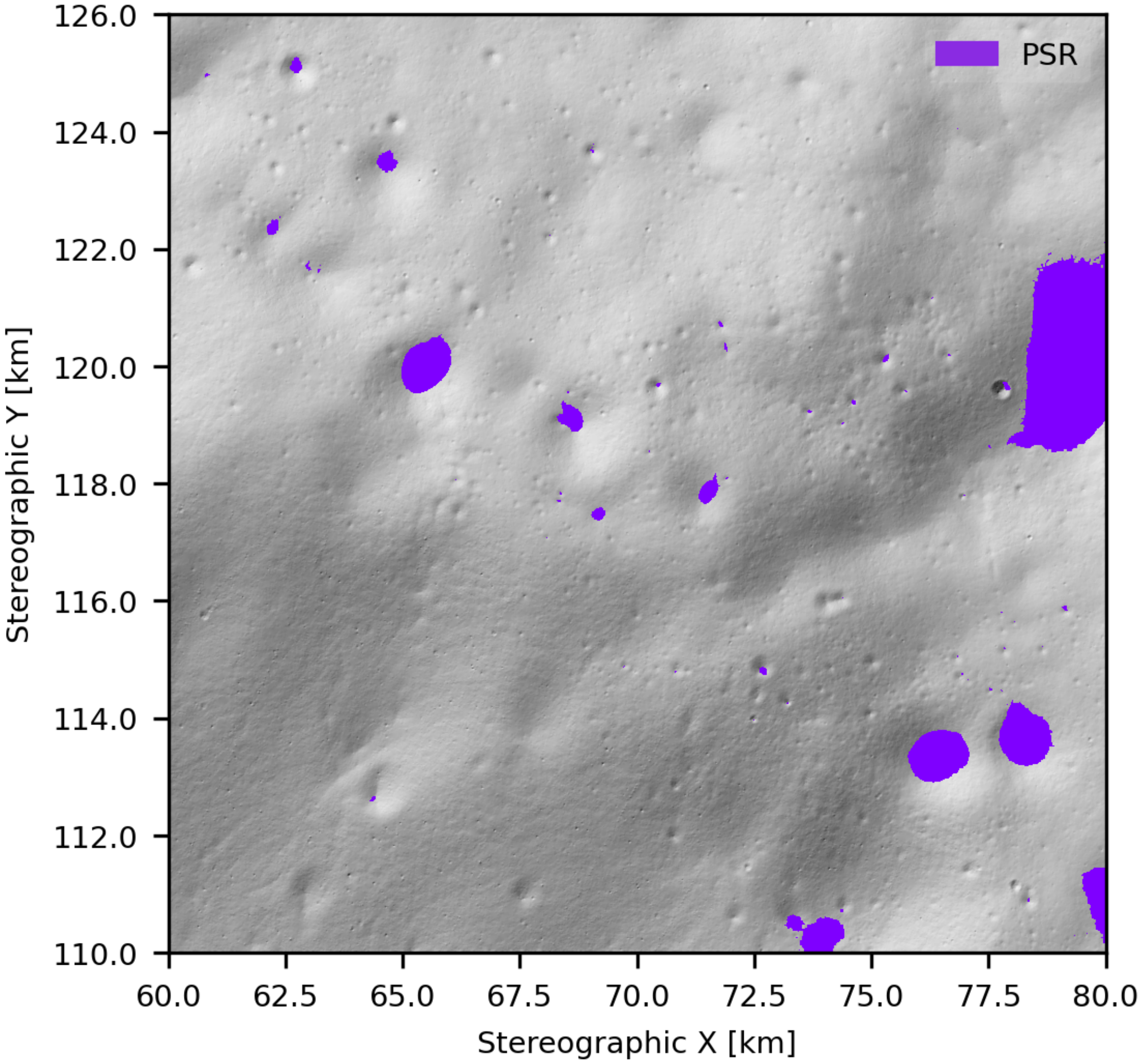

Figure 3.3: High-resolution PSR map of the VIPER site. The regions in purple are where ice can stably exist on the surface in this region of the Moon. The base layer is a hillshade map.

3.2 Monte Carlo Model Outcomes

3.2.1 Predictions of Ejecta Thickness Characteristics

I ran 50 cases in the Monte Carlo ejecta model and estimated that the average thickness of ejecta ranges from 0.1 to 113.4 m across the study grid. Figure 3.4 illustrates the spatial distribution of ejecta thickness estimation across the study area. Inside the VIPER primary mission area (marked by the black dashed box in Figure 3.4), the ejecta cover is modeled to be 0.9 to 59 m thick. The PSRs located within the primary mission area are blanketed by a 0.9 to 34 m thick ejecta cover. The ejecta simulation results predict that the rims of large craters host the thickest ejecta deposits while crater interiors are covered by comparatively sparse ejecta. The thickness of ejecta outside of craters remains the same in each model run but in crater interiors, the highest variation is observed (Figure 3.5). This is because the amount of ejecta deposited inside a crater depends on its time of emplacement which varies between each simulation case.

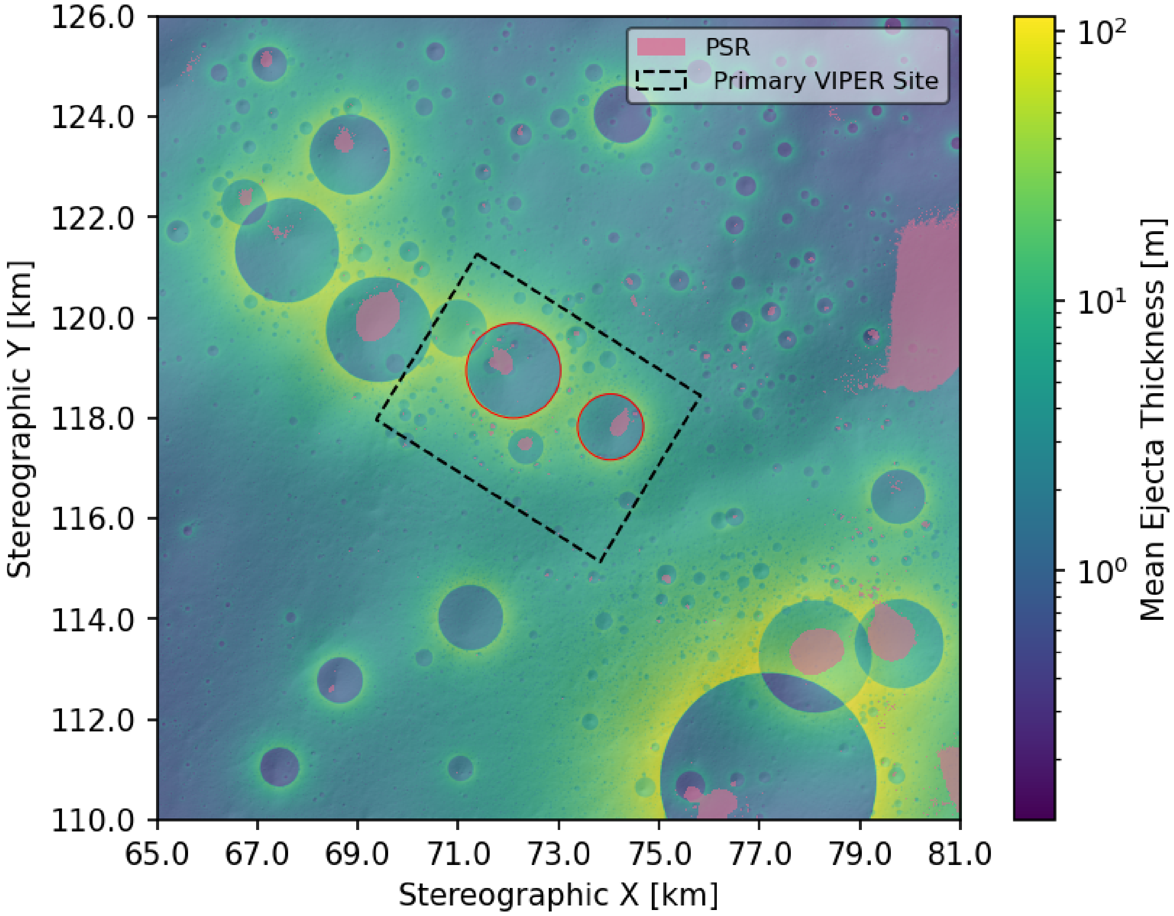

Figure 3.4: The spatial distribution of mean ejecta thickness predicted by the Monte Carlo model. The regions in permanent shadow derived from the illumination model are shown in pink. The primary mission area is indicated by the black dashed box. Red circles are large PSR hosting craters at the primary mission area. The spatial coordinates are in south-polar stereographic projection.

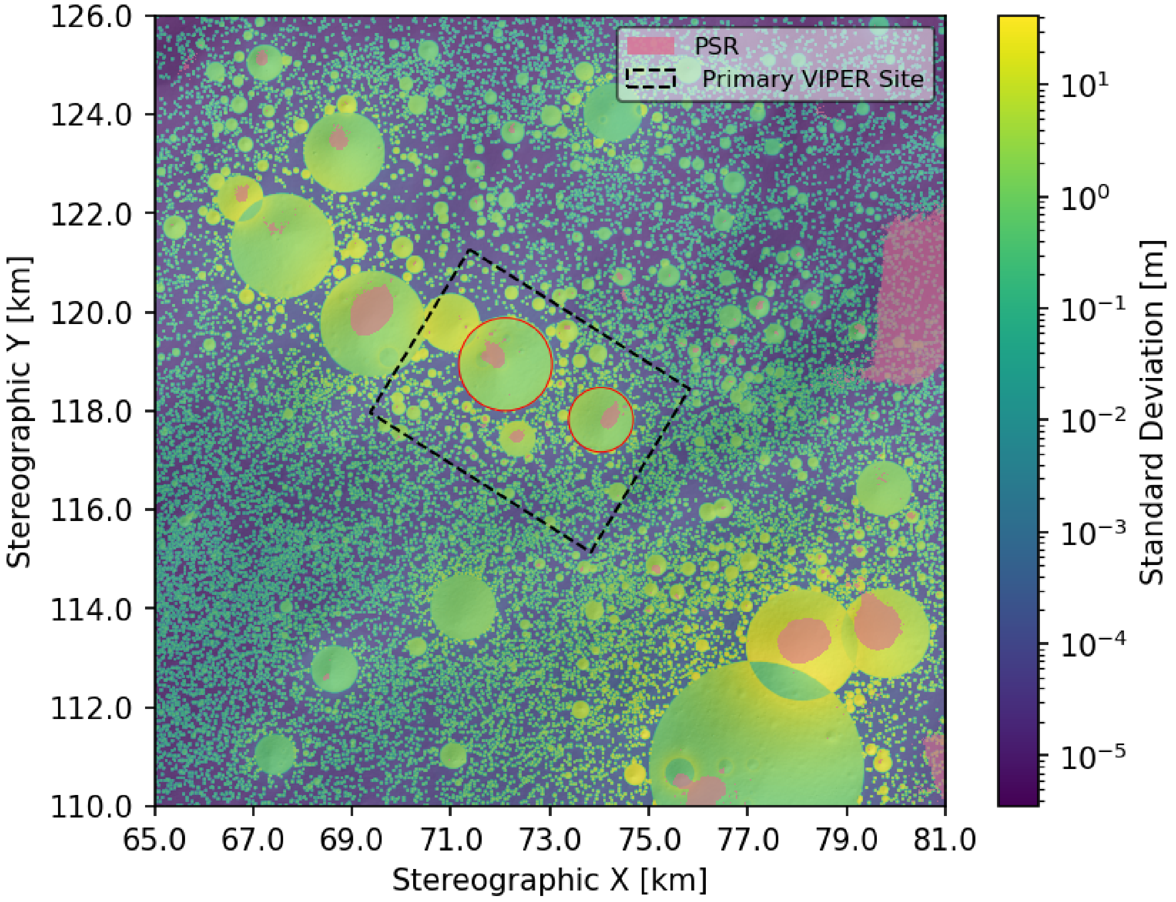

Figure 3.5: The map showing the standard deviation of ejecta thicknesses estimated by the simulation cases. Note that the crater interiors where PSRs are hosted have the highest uncertainty.

3.2.2 Ejecta Growth as a Function of Model Age

From the model cases, I report a ∼7.41 m of ejecta thickness averaged over the study grid. The variation in the mean ejecta thickness of the grid with respect to its surface age is shown by the green line in Figure 3.6. The Monte Carlo model results suggest that large amounts (∼4 m) of ejecta were deposited at the VIPER site in its early history (between 4 Ga and 3.75 Ga). It is followed by a rapid deceleration in the buildup of ejecta towards the present and only 1 m of cumulative ejecta has accumulated in the last 2.5 billion years. This observation is consistent with the decrease in regolith production rate with time derived analytically for the Apollo-15 landing site (Hirabayashi et al., 2018). A similar trend was observed when regolith thicknesses measured at Apollo and Chang'E mission sites by analyzing small crater morphometry were plotted against their corresponding model ages (Di et al., 2016). However, inside the primary mission area, relatively thicker ejecta is estimated (shown by the pink line in Figure 3.6) and a mean thickness of ∼11.06 m is modeled since its formation. This thicker estimate is likely due to the presence of many larger craters (diameter $>$ 1 km) inside the primary mission area. The model also yields an absolute model age of 4.086 Ga (error range: $+670$ Ma, -860 Ma) for the study grid based on the observed crater densities. This age estimate is consistent with the dating of the craters present within VIPER's primary mission area by Fassett et al. (2022) by quantifying the diffusive degradation of their rim features.

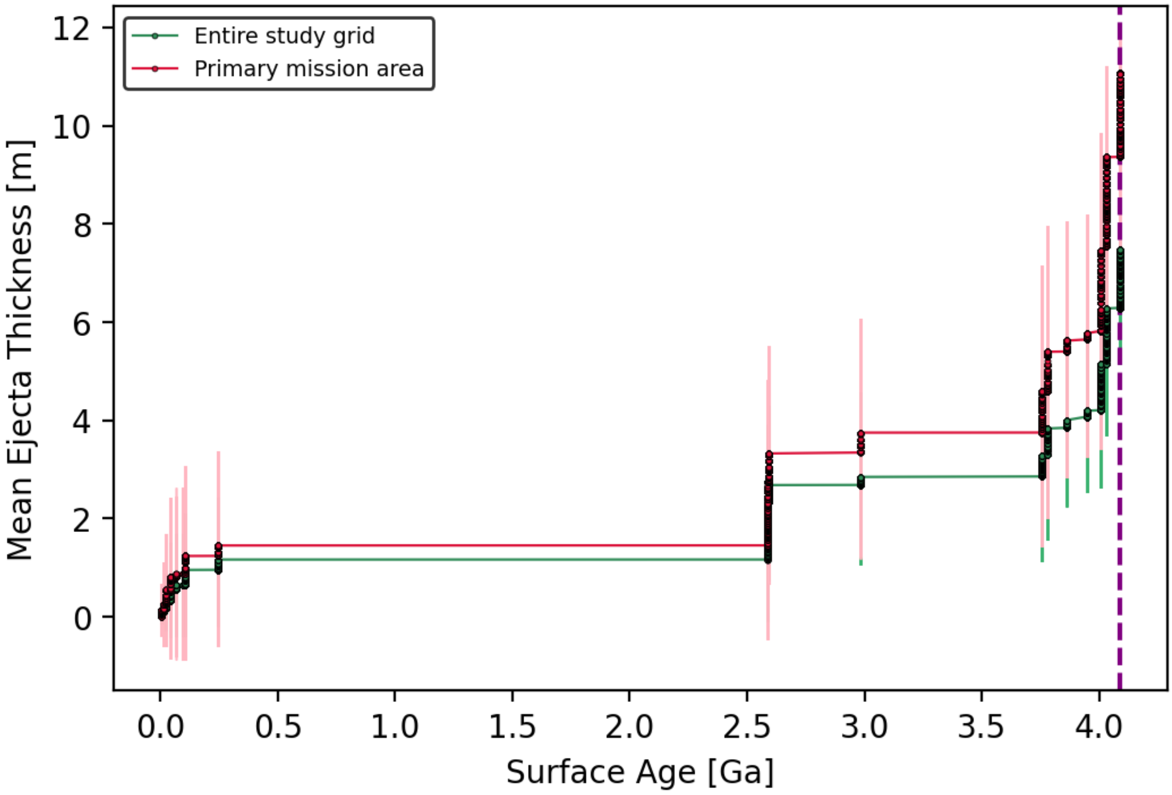

Figure 3.6: The mean ejecta thickness determined by the Monte Carlo numerical model is plotted as a function of surface age. The error bars indicate 1 standard deviation. The dashed purple line at 4.086 Ga refers to the VIPER site formation.

3.3 Comparison with Hirabayashi et al., 2018 Analytical Model

Next, I ran a comparison test with the analytical model for regolith production developed by Hirabayashi et al. (2018). Their model quantifies the amount of regolith produced by simple craters through ejecta blanketing on their exterior and brecciation on their interior. Hirabayashi et al. (2018) applied their model to the Apollo-15 landing site and validated the results with the regolith thickness measured via in-situ seismic experiments. I utilized their model to analytically derive the amount of regolith deposited by only the ejecta blankets of the VIPER crater population. I used the ejecta geometry coefficient from Pike (1974) (instead of Sharpton (2014)) to describe the ejecta blanket geometry in the analytical model because of its usage in my numerical simulations. At a time period T, the area fraction P_{out} at a depth h covered by ejecta-derived regolith is given by Equation 3.1. Parameters used in these expressions are detailed in Table 3.1.

$$\begin{aligned} P_{out} = 1 - \exp(-\frac{\xi X \eta \pi}{\eta - 2}\left\{(r^{out}_{max})^{-\eta+2} - (\frac{h_{out}}{\sigma})^{-\eta+2}\right\} + \\ \frac{\xi X \eta \pi}{\eta - 2 - \frac{2}{k}}\left(\frac{h_{out}}{\sigma}\right)^{-\frac{2}{k}}\left\{(r^{out}_{max})^{-\eta+2+\frac{2}{k}} - (\frac{h_{out}}{\sigma})^{-\eta+2+\frac{2}{k}}\right\}) \end{aligned} \tag{3.1}$$

Symbol	Parameter	Unit
ξ	coefficient of the visible crater CSFD	$m^{\eta-2}$
η	slope of the visible crater CSFD	no unit
X	normalized crater number	no unit
σ	ejecta blanket thickness at the crater rim as a fraction of crater radius	no unit
k	exponent indicating ejecta blanket thickness decay with distance	no unit
r^{out}_{max}	radius of the largest crater	km

Table 3.1: Parameters used in the analytical model of Hirabayashi et al. (2018).

h_{out} is obtained using Equation 3.2.

$$h_{out} = \begin{cases} h, & \text{if}\, h <= \sigma\, r^{out}_{max}; \\ \sigma\, r^{out}_{max}, & \text{if}\, h > \sigma\, r^{out}_{max}; \end{cases} \tag{3.2}$$

ξ and η are derived from the visible crater CSFD (C_t) measured at the VIPER site by using its expression (Equation 3.3) given in Hirabayashi et al. (2017).

$$C_t = A\xi X r_c^{-\eta} \tag{3.3}$$

The normalized crater parameter X is determined for time T as follows:

$$X = \frac{N(D)\,C(T)}{N(D)\,C(T = 4.086)} \tag{3.4}$$

Where $N(D)$ and $C(T)$ are lunar production and chronology functions expressed in equations 2.3 and 2.2 respectively in Chapter 2. Using Equation 15 in Hirabayashi et al. (2018) (Equation 3.1 in this document), I derived the fraction of area covered by ejecta at various depths during different timescales and it is shown in Figure 3.7.

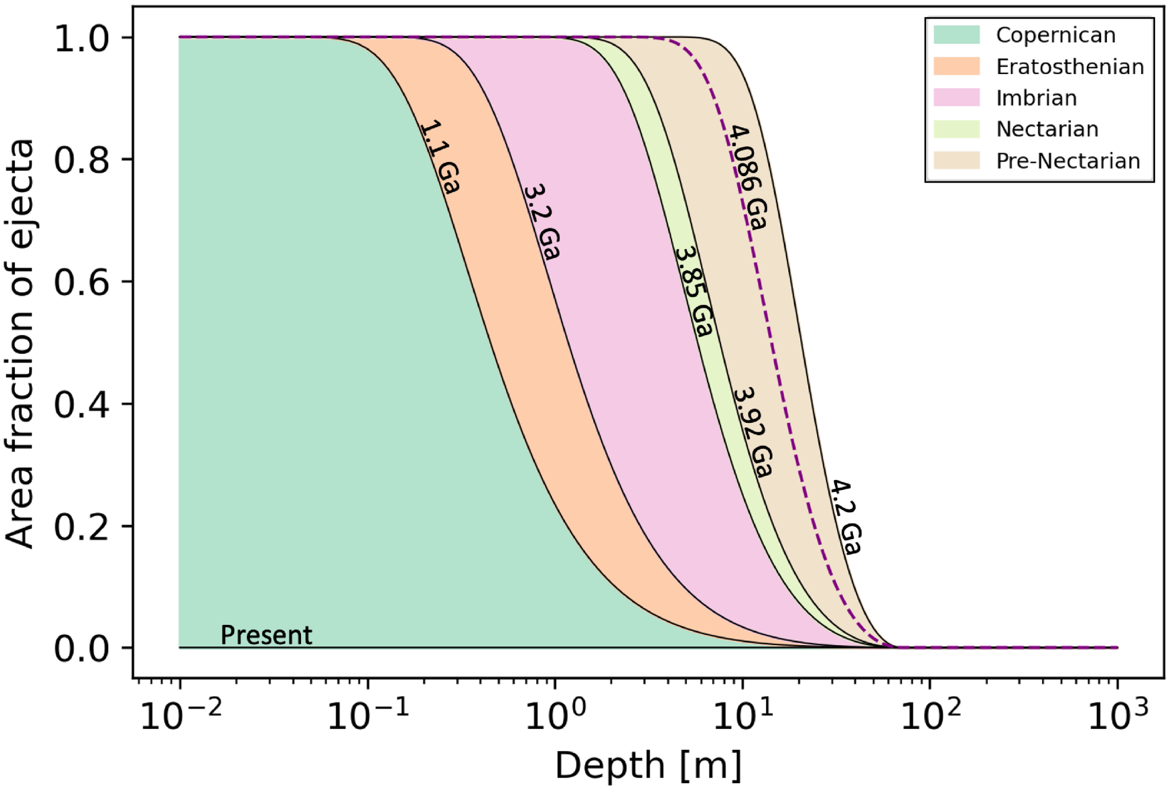

Figure 3.7: Area fraction covered by ejecta at different depths over geological timescales obtained using Hirabayashi et al. (2018) analytical model. The X-axis indicates the fraction of area filled by ejecta and the y-axis shows the depth. The graph is segmented into geological periods that are color-coded and the purple dashed line refers to the formation age of the VIPER site.

Since the beginning of the Nectarian period (3.92 Ga), 99% of the grid area was covered by ejecta up to ∼2.2 m depth, and nearly 1% of the area was covered by ejecta up to ∼48 m depth. Similarly, since the start of the Eratosthenian (3.2 Ga), ejecta filled 99% of the grid area up to ∼30 cm depth and 1% of the area up to ∼20 m depth. From the start of the Copernican period (1.1 Ga), ejecta filled 99% of the grid area up to ∼10 cm depth and 1% of the study area up to ∼10 m depth. I also determined the average ejecta thickness h_{av} at time T using Equation 18 (Equation 3.4 in this section) in Hirabayashi et al. (2018) and plotted it as a function of age in Figure 3.8.

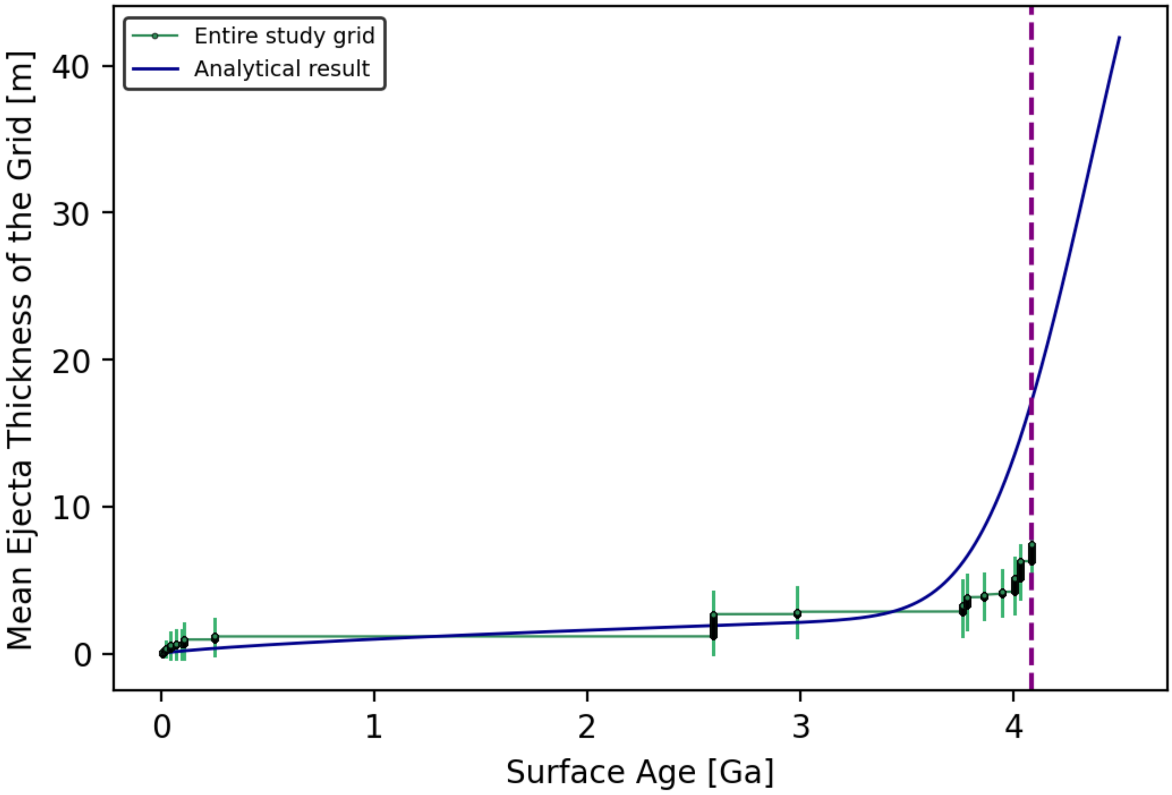

Figure 3.8: The mean ejecta thickness determined from the Monte Carlo numerical model (green line) plotted as a function of surface age compared with that derived using Hirabayashi et al. (2018) analytical model (dark blue line). The purple dashed line gives the formation of the VIPER site at 4.086 Ga.

$$h_{av} = -\int_{0}^{r_{max}^{out}} \frac{dP_{out}}{dh} h dh \tag{3.5}$$

For the last 3.5 Ga timescale, the average ejecta thickness h_{av} determined through the analytical model falls completely within 1 standard deviation of the Monte Carlo results as shown in Figure 3.8. However, for the timeframe before 3.5 Ga, the analytical model produces more mean ejecta across the grid. The average ejecta thickness h_{av} computed at 4.086 Ga is 17.25 m, i.e. $\sim$10 m more than the amount determined by the Monte Carlo model.

Chapter 4

Discussions

4.1 Spatial and Depth Distribution of Ejecta at the VIPER site

The Monte-Carlo ejecta model gives a constraint on the spatial distribution of ejecta thickness at the VIPER investigation area. Next, the model gives the average depth mixed at the VIPER site by ejecta blankets through time. The ejecta growth evolution modeled for the small crater population present at the VIPER site (shown in Figure 3.6) correlates with the decaying rates of impactor flux reaching the Moon over time (Neukum, 1983), and therefore, can be regarded as an indication of impact history at this location. However, there should be a considerable amount of ejecta contributed to the VIPER site from distal impacts in addition to the ejecta layering modeled in this study, specifically from the large, complex south polar craters that formed before and during the Imbrian period (Cannon et al., 2020). For example, the formation of Crater Amundsen (Diameter ∼51.7 km) during 3.9 Ga (Deutsch et al., 2020) would have deposited ∼188 m thick ejecta at the VIPER primary mission site. But it is likely that the majority of ejecta deposition during the Eratosthenian and Copernican occurred due to the small craters that are mapped in this study, and this allows the model results to fairly represent the structure of the shallow subsurface. This can also be confirmed by the strong agreement observed between the analytically derived ejecta thickness at ages younger than 3.5 Ga and the results from the numerical simulations shown in Figure 3.8. On the other hand, the difference between the results from the two models for the timeframe before 3.5 Ga could not be attributed to distal ejecta contamination since both models only compute ejecta generated from the input craters. Craters that got erased when the VIPER surface attained crater equilibrium are likely the sources of the missing ejecta. Additionally, the ejecta characteristics derived from the Monte Carlo model are affected by topographic diffusion and impact mixing due to small-scale craters that are not considered in this study. Therefore, the ejecta thickness estimates inferred from the model are likely the lower bound of the actual ejecta thickness at the VIPER site.

I do not find locations covered by ejecta thinner than 1 m. However, it is not necessary that the rover needs to penetrate through the entire ejecta cover to reach the bottom of the cold trap in order to seek ice because ice could have accumulated in between individual ejecta layers. The smallest crater size modeled here produced a maximum ejecta thickness of 60 cm. I suggest that such thin layers might constitute the structure of the top-meter regolith and might contain any recently delivered volatiles. While the structure of regolith in the inter-crater plains is consistent with the modeled ejecta layering, regolith that fills the crater interior also originates from mass-wasting processes from brecciation during the modification stage of cratering (Melosh, 1989; Hirabayashi et al., 2018) and from topographic diffusion that occurs when small craters form on existing crater walls (Fassett and Thomson, 2014; Talkington et al., 2022) aside from ejecta blanketing, which tends to further mix any ice accumulations. Such mass wasted regolith would amount to some portion of drill cores collected at PSRs which occur usually inside craters. Therefore, these model results cannot be equated with the real quantities of regolith present at the VIPER site.

4.2 Implications for the VIPER Mission

A considerable area of the study grid (as well as the primary mission area) is in permanent shadow where surface ice is stable and might be present. Using the Moon Mineralogy Mapper (M^3) empirical observations, Li et al. (2018) has detected surface ice at the large-scale PSR present outside the primary mission area. While Li et al. (2018) does not find surface ice inside the primary mission area, this could simply be due to resolution limits. The PSRs that are mapped inside the primary mission area are smaller than M^3 pixels (280 x 280 m) and any ice exposed on the surface might have been below the instrument's sensitivity limits. The upper 1 m of the VIPER subsurface where TRIDENT drill cores are to be collected consists of ejecta deposited during the Copernican period (the last 1.1 Ga). This regolith column might be devoid of ice for several reasons. The variation in volatile supply flux through time is not clearly understood yet but its decreasing trend has been generally recognized in previous studies. Ice supply flux in the Copernican is 100 times lower than what it was during Imbrian (Cannon et al., 2020; Lucey et al., 2022) owing to the decline in impactor flux reaching the Moon as well as the extinction of mare volcanism. Only 10^{18} g of volatiles (micrometeorites of $<$1 cm size = 10^{17} g, 1 cm to 1 m sized impacts = 10^{15} g, asteroids of $<$1 m size = 10^{18} g, comets = 10^{17} g, solar wind hydrogen = 10^{14} to 10^{15}, volcanism = 0) are delivered to the entire lunar surface in the Copernican according to Lucey et al. (2022). It is not clear how efficiently these volatiles were delivered to and retained in the polar cold traps given that the sources might not have been sufficiently intense to generate a transient atmosphere to facilitate the migration of the volatiles toward the traps. If they had been delivered to the VIPER site, their chances of survival until the present would then depend on the rates of impact gardening and space weathering since deposition. Costello et al. (2021)'s prediction that the top 1 m of the lunar surface would be gardened and dehydrated in the last 1 Ga eliminates the possibility of finding ice within the VIPER drill cores. Similarly, space weathering on icy regolith by the constant flux of solar wind and micrometeorites would remove the top layer ice. Unless the embedded volatiles are immediately buried by regolith sufficiently thick to shield from these erosional processes, they would be lost.

Alternatively, ancient buried ice (delivered prior to Copernican, and got buried under subsequent ejecta) might have been brought upward by impact mixing processes in case they had survived impact shock pressures (Costello et al., 2021) and could be present within VIPER's drilling depth. In this case, ejecta blankets can be interpreted as redistributors of ice rather than only shielding them from further erosion. Going deeper than 1 m, more ice can be expected (Colaprete et al., 2010; Cannon et al., 2020). Higher rates of volatile delivery by impacts and interior degassing could have supplied voluminous ice to the VIPER site during and before the Imbrian, which would occur buried under meters-thick ejecta as suggested by the model. At the same time, it is also possible that the VIPER site does not host bulky ice in the subsurface such as the gigaton deposits predicted by Cannon et al. (2020) because of the absence of large craters (kilometer scale), which are observed as favorable ice depositional environments in several studies (Cannon et al., 2020; Deutsch et al., 2020; Costello et al., 2021; Talkington et al., 2022). Moreover, the PSRs hosted inside the craters in VIPER's primary mission area (marked by red circles in Fig 1) are quite younger (3.6 - 3.7 Ga; Fassett et al. (2022)) and they postdate the periods of intense ice delivery in the Nectarian and Pre-Nectarian (Cannon et al., 2020). While these PSRs have likely avoided contamination from distal ejecta owing to their young age, they might not have accumulated substantial quantities (like meters-thick ice from Cannon et al. (2020)) of volatiles as well due to the same reason. However, this is suggested with caution since there is no clear relationship identified between the age of a cold trap and its ice volume (Deutsch et al., 2020). If the primary area PSRs contain some lenses of ice in the subsurface, the model results indicate that they are covered by ejecta of only a few meters thickness (up to 7 m; Refer to Figure 3.4). Given that impact gardening only removes volatiles in the upper 3 m over the past 3 Ga (Costello et al., 2021), they might be detected by VIPER's seismic sounding instrument which is capable of penetrating up to 5 m depth (Colaprete, 2022).

Tidal forces exerted in the Earth-Moon system have caused the orientation of the rotational axis of the Moon to fluctuate over time (Ward, 1975; Farhat et al., 2022). The Moon's current Cassini spin state was achieved 4.1 billion years ago after a major axial reorientation event. Its obliquity was $\sim 70°$ when the transition occurred and such high inclination would not have created persistent shadows in the poles, hindering their ice-trapping capacity (Ward, 1975; Schörghofer and Rufu, 2023). But the axial tilt has since decreased, reaching nearly $\sim 5.5°$ at 3.4 Ga when the first permanent shadows would have formed, but at scales much smaller than the current areal extent (Cannon and Deutsch, 2023; Schörghofer and Rufu, 2023). These latest studies also point out that the large quantities of volatiles delivered to the Moon in its early history could not have been retained due to the absence of polar cold traps at those times and therefore, the ice that we now observe must have been delivered recently, after the formation of the first cold traps in 3.4 Ga. Schörghofer and Rufu (2023) reported that the 5 wt% volatiles detected at Cabeus crater during the LCROSS mission could have been deposited only after 0.9 Ga based on their computations of lunar orbital evolution. Cannon and Deutsch (2023) also suggested that about 1 m of ice was supplied to the polar cold traps in the last 1.5 Ga and they might still be present if they had survived impact mixing whose intensity has largely diminished in the last billion years. Based on these recent developments, it can be suggested that there are high chances of finding young ice within VIPER's 1 m drill cores.

Chapter 5

Conclusion

Based on simulating the ejecta blankets of small craters present at the VIPER investigation area, I find that the top 1 meter of the surface where drill cores will be collected is composed of Copernican ejecta. The Monte Carlo model-derived ejecta growth is validated using a previously published analytical model (Hirabayashi et al., 2018) and a strong consistency is observed especially in the shallow subsurface stratigraphy. By mapping shadows over a lunar precession (~ 18.6 years), I deduce 0.5 km^2 of PSR area inside the rover's primary mission site where stable water ice could occur on the surface and if they exist, the spectrometers onboard VIPER would detect them. Nearly 0.9 to 59 m of ejecta covers the primary mission area and about 0.9 to 34 m thick ejecta fills the PSRs located there. While there are virtually no locations inside the primary mission area where the model-derived ejecta thickness is lower than 1 m (smaller than the drilling depth), ice is anticipated to be present in between ejecta layers of centimeter thickness. Latest research indicates that most of the ice detected at the lunar poles is younger. In that case, the chances of finding ice inside VIPER drill cores are high. Moreover, the estimates of ejecta thickness derived in this study are likely the lower bound of the actual regolith present at the VIPER site. Further modeling of regolith transport by impact-induced mass wasting on crater walls and gardening driven by small-scale craters that are not yet accounted for would provide a robust insight into the material distribution at the VIPER mission site.

References

Annex, A. M., Pearson, B., Seignovert, B., Carcich, B. T., Eichhorn, H., Mapel, J. A., Von Forstner, J. L. F., McAuliffe, J., Del Rio, J. D., Berry, K. L., et al. (2020). Spiceypy: A pythonic wrapper for the spice toolkit. *Journal of Open Source Software*, 5(46):2050.

Barker, M. K., Mazarico, E., Neumann, G. A., Smith, D. E., Zuber, M. T., and Head, J. W. (2021). Improved lola elevation maps for south pole landing sites: Error estimates and their impact on illumination conditions. *Planetary and Space Science*, 203:105119.

Butler, B. J. (1997). The migration of volatiles on the surfaces of mercury and the moon. *Journal of Geophysical Research: Planets*, 102(E8):19283–19291.

Cannon, K. M. and Britt, D. T. (2020). A geologic model for lunar ice deposits at mining scales. *Icarus*, 347:113778.

Cannon, K. M. and Deutsch, A. N. (2023). Revisiting ice stratigraphies at the lunar poles. In *54th Lunar and Planetary Science Conference*.

Cannon, K. M., Deutsch, A. N., Head, J. W., and Britt, D. T. (2020). Stratigraphy of ice and ejecta deposits at the lunar poles. *Geophysical Research Letters*, 47(21):e2020GL088920.

Colaprete, A. (2022). Viper: A lunar water reconnaissance mission. In *NASA Exploration Science Forum*.

Colaprete, A., Elphic, R., Shirley, M., Ennico-Smith, K., Lim, D., Zacny, K., Captain, J., Seigler, M., Balaban, E., Beyer, R and5, M. Z., Lees, D., and the VIPER Science Team (2023). Key science questions to be addressed by the volatiles investigating polar exploration rover (viper). In *54th Lunar and Planetary Science Conference*.

Colaprete, A., Schultz, P., Heldmann, J., Wooden, D., Shirley, M., Ennico, K., Hermalyn, B., Marshall, W., Ricco, A., Elphic, R. C., et al. (2010). Detection of water in the lcross ejecta plume. *science*, 330(6003):463–468.

Costello, E., Ghent, R., Hirabayashi, M., and Lucey, P. (2020). Impact gardening as a constraint on the age, source, and evolution of ice on mercury and the moon. *Journal of Geophysical Research: Planets*, 125(3):e2019JE006172.

Costello, E. S., Ghent, R. R., and Lucey, P. G. (2018). The mixing of lunar regolith: Vital updates to a canonical model. *Icarus*, 314:327–344.

Costello, E. S., Ghent, R. R., and Lucey, P. G. (2021). Secondary impact burial and excavation gardening on the moon and the depth to ice in permanent shadow. *Journal of Geophysical Research: Planets*, 126(9):e2021JE006933.

Crider, D. and Vondrak, R. (2002). Hydrogen migration to the lunar poles by solar wind bombardment of the moon. *Advances in Space Research*, 30(8):1869–1874.

Deutsch, A. N., Head III, J. W., and Neumann, G. A. (2020). Analyzing the ages of south polar craters on the moon: Implications for the sources and evolution of surface water ice. *Icarus*, 336:113455.

Di, K., Sun, S., Yue, Z., and Liu, B. (2016). Lunar regolith thickness determination from 3d morphology of small fresh craters. *Icarus*, 267:12–23.

Dreyer, C. B. (2021). Mining lunar polar ice for lo2/lh2 propellant. In *ASCEND 2021*, page 4235.

Farhat, M., Auclair-Desrotour, P., Boué, G., and Laskar, J. (2022). The resonant tidal evolution of the earth-moon distance. *Astronomy & Astrophysics*, 665:L1.

Farrell, W., Hurley, D., Poston, M., Hayne, P., Szalay, J., and McLain, J. (2019). The young age of the lamp-observed frost in lunar polar cold traps. *Geophysical Research Letters*, 46(15):8680–8688.

Fassett, C., Beyer, R., Colaprete, A., Coyan, J., Deutsch, A., Heldmann, J., Hirabayashi, T., Keszthelyi, L., and Lim, D. (2022). Age estimates for permanently shadowed craters in the viper mission area based on their topography. In *53rd Lunar and Planetary Science Conference*.

Fassett, C. I. and Thomson, B. J. (2014). Crater degradation on the lunar maria: Topographic diffusion and the rate of erosion on the moon. *Journal of Geophysical Research: Planets*, 119(10):2255–2271.

Gault, D., Hörz, F., Brownlee, D., and Hartung, J. (1974). Mixing of the lunar regolith. In *Lunar and planetary science conference proceedings*, volume 5, pages 2365–2386.

Grün, E., Horanyi, M., and Sternovsky, Z. (2011). The lunar dust environment. *Planetary and Space Science*, 59(14):1672–1680.

Head, J. W., Wilson, L., Deutsch, A. N., Rutherford, M. J., and Saal, A. E. (2020). Volcanically induced transient atmospheres on the moon: assessment of duration, significance, and contributions to polar volatile traps. *Geophysical Research Letters*, 47(18):e2020GL089509.

Hirabayashi, M., Howl, B. A., Fassett, C. I., Soderblom, J. M., Minton, D. A., and Melosh, H. (2018). The role of breccia lenses in regolith generation from the formation of small, simple craters: Application to the apollo 15 landing site. *Journal of Geophysical Research: Planets*, 123(2):527–543.

Hirabayashi, M., Minton, D. A., and Fassett, C. I. (2017). An analytical model of crater count equilibrium. *Icarus*, 289:134–143.

Hurley, D. M., Lawrence, D. J., Bussey, D. B. J., Vondrak, R. R., Elphic, R. C., and Gladstone, G. R. (2012). Two-dimensional distribution of volatiles in the lunar regolith from space weathering simulations. *Geophysical Research Letters*, 39(9).

Ivanov, B., Neukum, G., and Wagner, R. (2001). Size-frequency distributions of planetary impact craters and asteroids. *Collisional processes in the solar system*, pages 1–34.

Kornuta, D., Abbud-Madrid, A., Atkinson, J., Barr, J., Barnhard, G., Bienhoff, D., Blair, B., Clark, V., Cyrus, J., DeWitt, B., et al. (2019). Commercial lunar propellant architecture: A collaborative study of lunar propellant production. *Reach*, 13:100026.

Kring, D. A., Kramer, G. Y., Bussey, D. B. J., Hurley, D. M., Stickle, A. M., and van der Bogert, C. H. (2021). Prominent volcanic source of volatiles in the south polar region of the moon. *Advances in Space Research*, 68(11):4691–4701.

Li, S., Lucey, P. G., Milliken, R. E., Hayne, P. O., Fisher, E., Williams, J.-P., Hurley, D. M., and Elphic, R. C. (2018). Direct evidence of surface exposed water ice in the lunar polar regions. *Proceedings of the National Academy of Sciences*, 115(36):8907–8912.

Lucey, P. G., Petro, N., Hurley, D. M., Farrell, W. M., Prem, P., Costello, E. S., Cable, M. L., Barker, M. K., Benna, M., Dyar, M. D., et al. (2022). Volatile interactions with the lunar surface. *Geochemistry*, 82(3):125858.

McGetchin, T. R., Settle, M., and Head, J. (1973). Radial thickness variation in impact crater ejecta: Implications for lunar basin deposits. *Earth and Planetary Science Letters*, 20(2):226–236.

Melosh, H. J. (1989). Impact cratering: A geologic process. *New York: Oxford University Press; Oxford: Clarendon Press*.

Michael, G., Kneissl, T., and Neesemann, A. (2016). Planetary surface dating from crater size-frequency distribution measurements: Poisson timing analysis. *Icarus*, 277:279–285.

NASA (2020a). NASA's plan for sustained lunar exploration and development. Technical report, NASA.

NASA (2020b). NASA's Lunar Exploration Program Overview. Technical report, NASA.

Needham, D. H. and Kring, D. A. (2017). Lunar volcanism produced a transient atmosphere around the ancient moon. *Earth and Planetary Science Letters*, 478:175–178.

Neish, C., Bussey, D., Spudis, P., Marshall, W., Thomson, B., Patterson, G., and Carter, L. (2011). The nature of lunar volatiles as revealed by mini-rf observations of the lcross impact site. *Journal of Geophysical Research: Planets*, 116(E1).

Neukum, G. (1983). Meteoritenbombardement und datierung planetarer oberflachen. *Habilitation Dissertation for Faculty Membership, Ludwig-Maximilians-Univ.*

Oberbeck, V. R. and Quaide, W. L. (1968). Genetic implications of lunar regolith thickness variations. *Icarus*, 9(1-3):446–465.

Ong, L., Asphaug, E. I., Korycansky, D., and Coker, R. F. (2010). Volatile retention from cometary impacts on the moon. *Icarus*, 207(2):578–589.

Paige, D. A., Siegler, M. A., Zhang, J. A., Hayne, P. O., Foote, E. J., Bennett, K. A., Vasavada, A. R., Greenhagen, B. T., Schofield, J. T., McCleese, D. J., et al. (2010). Diviner lunar radiometer observations of cold traps in the moon's south polar region. *science*, 330(6003):479–482.

Pike, R. J. (1974). Ejecta from large craters on the moon: Comments on the geometric model of mcgetchin et al. *Earth and Planetary Science Letters*, 23(3):265–271.

Prem, P., Artemieva, N., Goldstein, D., Varghese, P., and Trafton, L. (2015). Transport of water in a transient impact-generated lunar atmosphere. *Icarus*, 255:148–158.

Rubanenko, L., Venkatraman, J., and Paige, D. A. (2019). Thick ice deposits in shallow simple craters on the moon and mercury. *Nature Geoscience*, 12(8):597–601.

Schultz, P. H., Hermalyn, B., Colaprete, A., Ennico, K., Shirley, M., and Marshall, W. S. (2010). The lcross cratering experiment. *science*, 330(6003):468–472.

Schörghofer, N. and Rufu, R. (2023). Past extent of lunar permanently shadowed areas. In *54th Lunar and Planetary Science Conference*.

Sharpton, V. L. (2014). Outcrops on lunar crater rims: Implications for rim construction mechanisms, ejecta volumes and excavation depths. *Journal of Geophysical Research: Planets*, 119(1):154–168.

Shoemaker, E. M. (1966). Progress in the analysis of the fine structure and geology of the lunar surface from the ranger viii and ix photographs.

Sowers, G. F. and Dreyer, C. B. (2019). Ice mining in lunar permanently shadowed regions. *New Space*, 7(4):235–244.

Stewart, B. D., Pierazzo, E., Goldstein, D. B., Varghese, P. L., and Trafton, L. M. (2011). Simulations of a comet impact on the moon and associated ice deposition in polar cold traps. *Icarus*, 215(1):1–16.

Talkington, C., Hirabayashi, M., Montalvo, P., Deutsch, A., Fassett, C., Siegler, M., Shepherd, S., and King Jr, D. (2022). Survival of ancient lunar water affected by topographic degradation of old, large complex craters. *Geophysical Research Letters*, 49(15):e2022GL099241.

Thomson, B., Bussey, D., Neish, C., Cahill, J., Heggy, E., Kirk, R., Patterson, G., Raney, R., Spudis, P., Thompson, T., et al. (2012). An upper limit for ice in shackleton crater as revealed by lro mini-rf orbital radar. *Geophysical Research Letters*, 39(14).

Ward, W. R. (1975). Past orientation of the lunar spin axis. *Science*, 189(4200):377–379.

Watson, K., Murray, B., and Brown, H. (1961). On the possible presence of ice on the moon. *Journal of Geophysical Research*, 66(5):1598–1600.